PHYSICS IV 2001
Research Project Report

Modelling Pulsar/Be Star Binary System
PSR B1259−63/SS2883
Periastron and Eclipse in 2000

Tim Connors
School of Physics
University of Sydney
email:tcon@physics.usyd.edu.au

Abstract

PSR B1259−63 is a radio pulsar in orbit about the Be star SS2883. The orbit is highly elliptical with a period of 3.4 years. Around the time of closest approach ("periastron", denoted $\mathcal{T}$) of the two stars, the system becomes a radio, X-ray and γ-ray transient. I have analysed a sequence of 30 independent observations at 4 radio frequencies made with the Australia Telescope Compact Array (ATCA) during the late 2000 periastron passage to monitor the radio continuum transient. The light curves produced from the data are then compared with the 1997 periastron and with the predictions of a synchrotron bubble model. Similarities and differences are discussed in detail.

I analysed polarization data from the pulsar to obtain rotation measures at a number of epochs. The value of -16600 ± 1700 rad m^{-2} during part of the September 1 ($\mathcal{T} - 46$) observation is the largest astrophysical RM ever measured. I discuss the implication of this for the magnetic field in the Be star's wind.

Acknowledgements

I would like to thank my supervisor Simon Johnston for performing most of the observations, for the data and initial scripts to flag, calibrate and image the data, and fit the RM to the pulsar data, as well as, of course, providing plenty of help and suggestions during the project — especially in trying to improve my error analysis, and proofreading of the almost final thesis. I will also thank the various honours students on this floor (and indeed everyone elsewhere), for providing mutual support during those times of crisis otherwise known as "assignment due date".

Thanks also to Richard Hunstead for providing much help during late nights – such as finding obscure Fortran books for equally obscure Fortran commands.

I also have to thank T. I. Elcaro, for insightful conversations, and family and friends outside University life who have kept me going all this time.

I certify that this report contains work carried out
by myself except where otherwise acknowledged.

Signed: ....
October 19, 2001

Contents

Chapter 1

Introduction

1.1 Pulsars

1.1.1 History

Pulsar physics started with Chinese astronomers, who saw a "guest star" (or supernova) in 1054AD, that was later associated with the Crab nebula. Neutron stars were theorised about in 1934 (Baade & Zwicky 1934a), and the Crab nebula contained a faint blue star which was thought to be a neutron star (Baade & Zwicky 1934b):

> With all reserve we advance the view that supernovae represent the transitions from ordinary stars into neutron stars, which in their final stages consist of extremely closely packed neutrons.

The first attempts at modelling their properties began in 1939 (Oppenheimer & Volkoff 1939). A neutron star is a star that was once more massive than about $8M_\odot$ (where $\odot$ denotes the Sun), that came to the end of its hydrogen burning phase, and has collapsed into a super dense object about 20km across, and a mass of $\sim 1.4M_\odot$.

For 30 years, it was thought neutron stars would be very difficult to detect, but the first pulsar (CP 1919) was discovered by Jocelyn Bell in 1967 in Cambridge, England, while she was trying to find quasars using the scintillation of small sources (Hewish et al. 1968). In 1968, the star at the centre of the Crab nebula was determined to be a pulsar — PSR B0531+21 (Staelin & Reifenstein 1968; Reifenstein, Brundage & Staelin 1969).

After the discovery of CP 1919, Gold (1968) proposed a model of pulsars — a pulsar is a neutron star, that has a magnetic dipole that is misaligned with the rotational axis, with a beam of radiation at the pole being visible as it sweeps over the earth (e.g. Gold 1968; Gold 1969; Pacini 1968). With both the links between the Crab nebula neutron star and the supernova explosion, and between neutron stars and pulsars, the processes behind supernovae explosions and pulsars were well explained.

Since the first few discoveries, more than 1300 pulsars have been discovered mainly at radio wavelengths, and they show a wide variety of behaviours (Manchester 2001). Pulsars are most often seen at radio wavelengths, but also occasionally emit in other bands including optical, X-rays and γ-rays, with the emission mechanism still poorly understood (Melrose 1996).

1.1.2 Characteristics

Immediately after a supernova explosion, the angular momentum of a neutron star is conserved. The Crab pulsar PSR B0531+21 (the best example, since it is the youngest known pulsar) may have rotated hundreds of times per second at birth (Atoyan 1999). Similarly, the magnetic field,

B, at the surface of neutron stars increase from their stellar values through the conservation of magnetic flux, and lie between 10^4 and 10^9 Tesla (Johnston 1995).

The period of rotation is denoted P, and since the pulsar loses rotational energy from relativistic particles that stream outwards along the magnetic field lines, it slows down, and has a period derivative $\dot{P}$. PSR B0531+21 now rotates 30 times a second, so has received significant slowdown over the last thousand years. The observed periods of pulsars range from about 0.001 to 8.5 seconds (Young, Manchester & Johnston 1999), and most probably, pulsars begin their lives spinning rapidly, then slow down gradually to rotate less than once per second. The pulsar will eventually cross the death line, where the voltage ($V \propto B/P^2$) above the polar cap is below a critical value, and is not high enough to sustain cascaded pair production, and the emission stops (Bhattacharya & van den Heuvel 1991). A binary pulsar may then eventually accrete matter from its companion, and spin back up from the extra angular momentum acquired (for a review of evolution, see Bhattacharya & van den Heuvel 1991 and references therein). These rejuvenated pulsars tend to rotate with periods in the tens of millisecond range, and are called millisecond pulsars.

The age for pulsars less than $\sim 10^6$ yr old, that have not been spun up, can be approximated by the characteristic age

$$\tau_{\mathrm{c}} = \frac{1}{n-1} \left(\frac{P}{\dot{P}} \right) \tag{1.1}$$

however, this breaks down for older pulsars[1] (Lyne, Ritchings & Smith 1975). The parameter n is 3 for a magnetic dipole braking, and measured to be 2.4 for the Crab pulsar.

The pulses suffer a delay dependent upon the radio frequency, from dispersion in the interstellar medium (Lyne & Smith 1968). The dispersion measure is defined by

$$\mathrm{DM} = \int_{\mathrm{LOS}} n_{\mathrm{e}}\, \mathrm{d}l \qquad (\mathrm{cm}^{-3}\mathrm{pc}) \tag{1.2}$$

where n_{e} is in cm^{-3}, l is in pc, and LOS denotes integration over the line of sight from observer to pulsar. Across the bandwidth of a receiver, the DM can be measured, and $\overline{n_{\mathrm{e}}}$ can be obtained, since the time of arrival $t = 4.15\,\mathrm{DM}\,\nu_{\mathrm{MHz}}^{-2}$ s implies the time delay $\Delta t = 8.3 \times 10^3\,\mathrm{DM}\,\nu_{\mathrm{MHz}}^{-3}$ ms/MHz, where ν_{MHz} is the frequency observed in MHz (Smith 1977, p142).

Linearly polarized radiation from the pulsar will also suffer Faraday rotation, and the rotation measure is given by

$$\mathrm{RM} = 8.1 \times 10^5 \int_{\mathrm{LOS}} n_{\mathrm{e}} \boldsymbol{B} \cdot \mathrm{d}\boldsymbol{l} \qquad (\mathrm{rad\,m^2}) \tag{1.3}$$

where $\boldsymbol{B}$ is in Gauss. The RM describes how much Faraday rotation will be applied to a linearly polarized source. Since pulsars are polarized, they usually are good sources to probe the mean magnetic field projected radially towards the Earth ($\overline{B\cos\theta}$, weighted as the number density), once the number density is known from the DM measurement, over the line of sight, as

$$\langle B_{\parallel} \rangle = 1.2 \frac{\mathrm{RM}}{\mathrm{DM}} \qquad (\mu\mathrm{G}) \tag{1.4}$$

The Faraday rotation angle depends on wavelength, such that

$$\Delta\phi = \mathrm{RM}\,\lambda^2 \tag{1.5}$$

---

[1] Lyne, Ritchings & Smith (1975) allow the magnetic field of the pulsar to decay exponentially, in which case the true age $\tau = \frac{1}{2}\tau_{\mathrm{D}} \log_{\mathrm{e}}(\frac{2\tau_{\mathrm{c}}}{\tau_{\mathrm{D}}} + 1)$, where τ_{D} is the time constant of the magnetic field $\sim 10^6$ yr. Using this, the maximum age is more realistic at $\sim 10^7$ yr, rather than $\sim 10^9$ yr .

where ϕ is the observed position angle (equation 3.1), and λ is the wavelength in meters.

Since there is a modulo π ambiguity in the position angle, care must be taken when finding the RM, since the angle may rotate many times within the observing bandwidth. The bandwidth can be split into many sections, and as long as there is enough spectral resolution, the rotation measure can be uniquely determined.

Generally, the DM and RM do not vary with time for pulsars, but as discussed in sections 2.3.1 and 2.3.2, they do for PSR B1259−63, and together form an excellent probe to the wind of the the Be star.

1.1.3 Pulsar winds

A large portion of the spin down energy of pulsars are in the form of relativistic electron and positron, and possibly ion winds.

Pulsars, especially those within supernova remnants such as the PSR B0531+21, can have fast flowing winds with several shock fronts, such as a MHD shock and a shock between the supernova remnant and interstellar medium (Kennel & Coroniti 1984). Wind from pulsars in binary systems may collide with the wind from the companion, causing a bow shock to be produced.

1.2 Be stars

Be stars are non-supergiant B type, or hot early type stars, with a circumstellar equatorial disk (Johnston et al. 1994). The principle and unique characteristic of Be stars, is that they show emission lines, originating from the disk (for an explanation of the varying spectra of Be stars, see Clingempeel 2001 and Buil 2000). The disk may be related to the fact that these stars rotate very quickly, $\sim 90\%$ of their breakup speed, where the centrifugal force is almost as strong as the gravitational force. There are signs that these stars may be unstable, as some of them suffer from outbursts, similar to solar flares. The stars typically rotate with a velocity of 345 km s^{-1}, and the disk possesses a Keplerian velocity distribution of the same order as the star's velocity.

Be stars form only 15% of all non-supergiant B stars, which are already relatively rare. They form in binaries when large amounts of matter and angular momentum are transfered from the primary to the secondary (van Kerkwijk 1993, pp139..171). Their radius is $\sim 6R_\odot$ and mass $\sim 10M_\odot$.

The general view (e.g. Underhill & Doazan 1982; Waters 1986; Waters, Coté & Lamers 1987 and references therein) is that there is a hot ($\sim 10^5 - 10^6$ K) tenuous (less than 10 times as dense than the disk) fast moving (~ 1500 km s^{-1}) wind which originates from the poles. The disk by comparison is a lot cooler ($\sim 10^4$ K), denser ($10^{-12} - 10^{-11}$ g cm^{-3}) and slower mostly Keplerian rotational motion, with a small (5 km s^{-1} at the star surface) radial outflow. The disk can be modelled simply by a small number of parameters — a half-opening angle of order $\sim 5 - 15°$, and two separate radial power law density distributions for the disk and polar wind:

$$n_e(r) = n_0(r/R_*)^{-\beta} \tag{1.6}$$

The density law implies a similar power law for the outflow velocity

$$v(r) = v_0(r/R_*)^{+\beta-2} \tag{1.7}$$

where $\beta \sim 2.75$. The mass density ρ can be substituted instead of electron number density n_e.

1.3   Binary Pulsar Evolution

There are a number of known systems where a neutron star orbits another star. These systems are usually either high mass X-ray binaries (HMXB), or low mass X-ray binaries (LMXB), although only HMXB will be discussed further here. HMXB are bright in X-rays because of the influx of matter onto the neutron star from the accretion disk.

Initially, in a binary star system, when the first neutron star forms, the system can take 2 paths. The most likely outcome is the stars separate — an explosion that either ejects enough of the star mass, or is suitably asymmetrical will give the neutron star more energy than binds it to the system. If the orbit of the two stars is circular, the mass loss is sufficiently fast, and the proportion of mass loss from the exploding star is greater than 0.5, then the system becomes unbound (Smith 1977, pp214..217). Other factors such as a collision of the expanding shell with the companion star can affect this result, but the exploding star having a mass of less than 0.2 of the companion, or ejecting less than 0.2 of its own mass guarantees the system remains bound (McClusky & Kondo 1971).
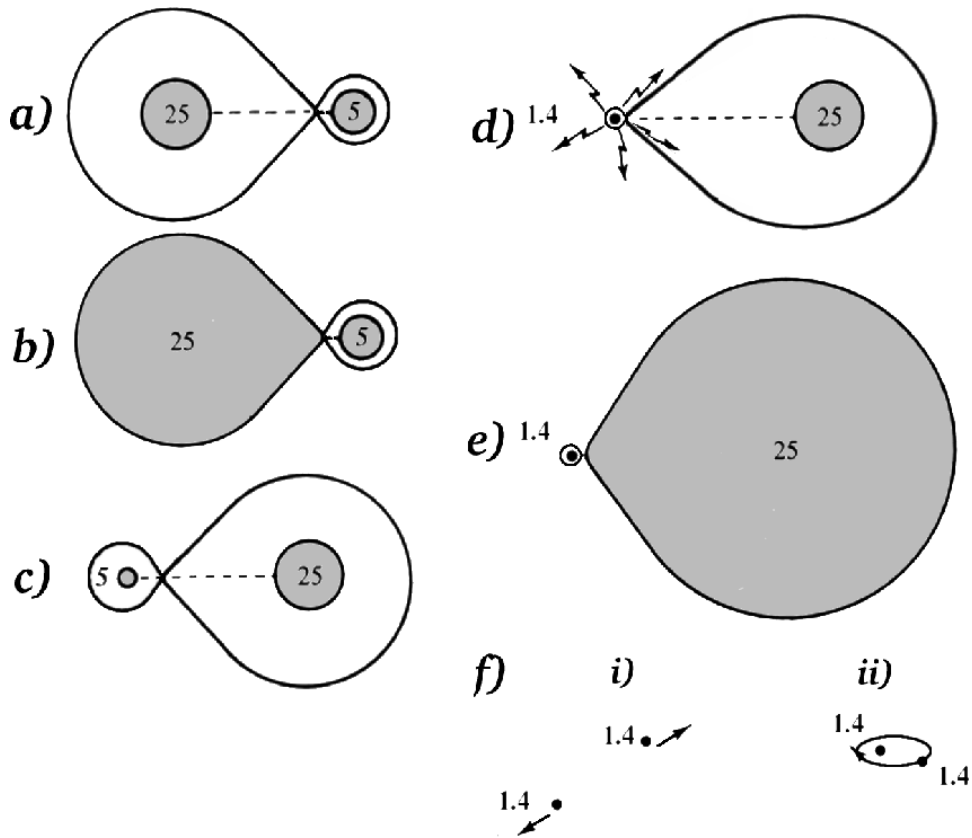
Figure 1.1: *Evolution of a neutron binary system. Outer surface is Roche-lobe, dark shading represents stellar material. The numbers shown are the masses in units of the solar mass, $M_\odot$. See text for explanation of evolution.*

A general overview of binary pulsar evolution is presented in Bhattacharya & van den Heuvel (1991), and we outline the path of interest to us below. Before either star in the system has evolved (figure 1.1a, where all masses shown are chosen to reflect those appropriate in the PSR B1259−63/SS2883 system, which are discussed in section 2.2), there will be a small amount of mass exchange. Before the supernova explosion, the initially massive star (herein referred to as the primary — the less massive star is the companion) may lose most of its mass (figure 1.1b) to the lighter companion during the red-giant phase, or even earlier, if the binary orbit is suffi-

ciently small (Lewin & van den Heuvel 1983, pp304–341), if it fills its Roche-lobe[2], and will be left with just a bright super-hot helium core (figure 1.1c) — a Wolf-Rayet star (van den Heuvel & de Loore 1973; de Loore, de Greve & Vanbeveren 1978). This star is light enough now, that when it explodes as a supernova it may not disrupt the system. If they stay together, the now heavier companion will very slowly lose mass to the pulsar (figure 1.1d), but may quickly lose mass through a high radiation pressure. This phase lasts $\sim 10^7$ yr (Tauris & Bailes 1996) before the companion star evolves, where it may then become a red giant for $\sim 10^4$ yr (figure 1.1e) overflowing its Roche-lobe, and then exploding as a supernova. The system will usually separate, with the two condensed objects (neutron stars, white dwarfs or black holes) separating with their typical orbital velocity (figure 1.1f.i), or the companion may have lost enough of its mass as a red-giant, that they stay bound after the second explosion, as a condensed star binary system (figure 1.1f.ii), such as the binary neutron star system, PSR B1913+16 (Taylor, Fowler & McCulloch 1979, and references therein).

---

[2]The surface defined by the equipotential surfaces of the two stars, that meet at the Lagrange point L_1. If the primary star fills the Roche-lobe, then unbalanced pressure at L_1 will cause mass transfer from the primary to the secondary (Tauris & Bailes 1996).

Chapter 2

Binary pulsar/Be star system (PSR B1259−63/SS2883)

PSR B1259−63 is a pulsar that orbits a Be star, SS2883. It was discovered in 1990, in a Parkes radio pulsar survey (Johnston et al. 1992). PSR B1259−63/SS2883 was the first pulsar and high mass star system, and is still unique, in that it is the only known system with a radio pulsar orbiting a Be star, although there are other binary systems involving X-ray emission and a neutron – Be star binary, and one very similar system, PSR J0045−7319, which involves a normal $\sim$ $9M_\odot$ B star (without a disk) and pulsar with an eccentric orbit with $e = 0.8$ (Kaspi et al. 1994; Kaspi, Tauris & Manchester 1996). PSR B1259−63 fills a missing link in the evolution of binary neutron star systems.

This system is quite young, and its state is described in figure 1.1d, with no accretion. It is thought to be a X-ray binary progenitor — it is expected that it will eventually evolve into the more oft seen HMXB.

2.1 Basic Properties

PSR B1259−63 is a young pulsar, with a period of ~ 48 ms. Johnston et al. (1994) suggest it is unlikely that significant spin up has occurred, through the action of accretion onto the pulsar. In fact, accretion onto the pulsar is probably not possible since the corotation velocity at the alfvén radius (the radius at which the radial component of the alfvén velocity is equal to the pulsar wind outflow radial velocity) is greater than the Keplerian velocity of in-streaming matter (Wex et al. 1998).

The dispersion measure of the pulsar is 146.7 cm^{-3}pc and the rotation measure is +21 rad m^{-2} away from periastron, when the pulsar is not affected by the Be star's atmosphere. These are presumably the values that the galactic interstellar medium contribute — sections 2.3.1 and 2.3.2 detail how these change over the orbit, and it is the difference from the galactic values which we are interested in. The dispersion measure, when combined with a model of galactic electron density, implies a distance of 4.6 kpc (Johnston et al. 1994).

The pulse profile (figure 2.1) has two almost equal intensity peaks (or components), which probably result from beams from the edges of a cone-shaped emission region (Manchester & Johnston 1995). The characteristic age of PSR B1259−63 is 0.33 Myr, and the magnetic field at the surface is 3.3×10^{11} G (Johnston et al. 1994). The pulses are usually highly polarized but become depolarized when scattered within the disk at periastron. The leading pulse is not circularly polarized, but the trailing pulse is.

The pulsar orbits the Be star with a period of about 3.4 years, and the orbit is the most highly eccentric of any known neutron star system, with $e = 0.87$ (Wex et al. 1998). The pulsar will
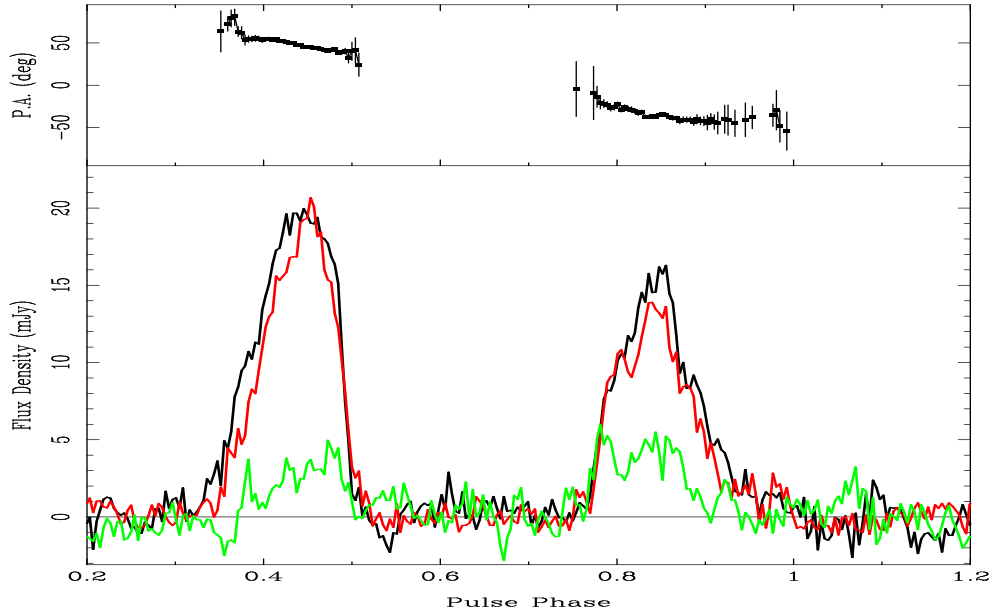
Figure 2.1: *Mean pulse profile from a March 30, 2001 observation at Parkes at 1.4 GHz (Johnston 2001, private communication). Position angle (equation 3.1) for significantly polarized flux is shown in top, and the Stokes I (black), V (green), and linear polarization $L = \sqrt{Q^2 + U^2}$ (red) are shown in bottom plot. Pulse component 1 flux densities: $I = 2.14$ mJy, $L = 86.5\%$, $V = 12.5\%$ Pulse component 2 flux densities: $I = 1.60$ mJy, $L = 86.6\%$, $V = 34.6\%$*

spend most of the 3.4 year orbit far from Be star, but for 50 days it travels through and then behind the disk, which eclipses and otherwise affects (along with the polar wind) the propagation of the radio signals from the pulsar.

Johnston et al. (1994) and Melatos et al. (1995) derived some properties of the Be star from optical observations. Timing of the pulsar gave a position and error that was consistent with an optical identification of a Be star SS2883, of magnitude 10.1, mass $\sim 10 M_\odot$ and radius $6 R_\odot$. Its type is probably B2e, which puts its absolute visual magnitude around -2.2 to -4.3, and hence its distance at 600 to 1600 pc. The dispersion measure combined with the distance of 1600 pc gives a mean electron number density in the line of sight of 0.1 cm^{-3}, 3 times higher than what is expected for this direction. The high DM may be due to an inappropriate galactic spiral arm model, or matter associated with the Be star, at a much larger scale than the pulsar orbit, since there is not much variation in the DM over the orbital period.

Spectral analysis of the Be star reveal it to be approaching us at about 80 km s^{-1}, which is much larger than typical B star velocities, and the 10 km s^{-1} expected from differential galactic rotation, and is possibly induced by the kick from the supernova explosion. Since the disk has a Keplerian velocity profile, the radius of emission of various emission lines can be deduced from the Doppler splitting of the lines, since the velocity of the disk is large and of the order of 150 km s^{-1} (Wex et al. 1998). Hβ is emitted from $8.5 R_c$, where $1 R_c$ is the radius of the companion, and the radius decreases for higher order Balmer lines, down to $3.3 R_c$ for Hδ. The star rotates with a projected velocity of $v \sin i_{\text{Be}} = 180$ km s^{-1}, implying a possible inclination angle i_{Be} of 40° with respect to the plane of the sky, since it is thought to rotate at 70% of the breakup velocity of 400 km s^{-1}. This is certainly not inconsistent (Melatos, Johnston & Melrose 1995) with the 36° obtained for the inclination angle i of the binary orbit from spectral type and stellar mass arguments, as the angle between the Be star's axis and the binary orbit, i_D is thought to be large (figure 2.2) — the disk is almost perpendicular to the orbit (Johnston et al. 1999).

The polar wind from the Be star is much faster ($\gtrsim 1000$ km s^{-1}) that the pulsar orbital velocity ($\lesssim 85$ km s^{-1}), so we expect the interface between the wind from the pulsar and Be star
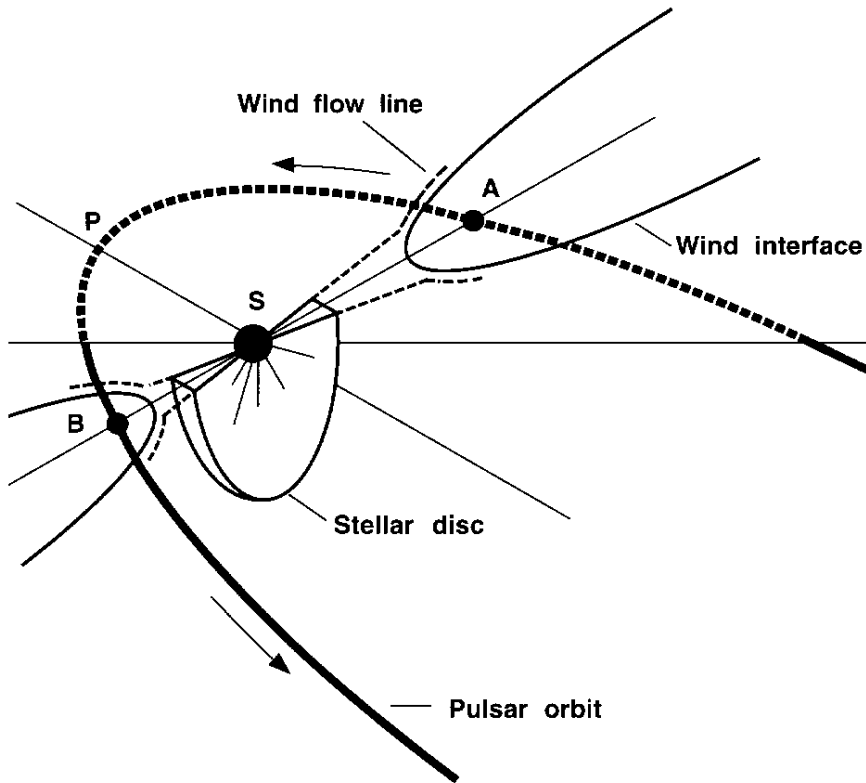
Figure 2.2: *Model from the 1997 periastron data, of the PSR B1259−63/SS2883 orbit. The Be disk is inclined at some angle i_D to the orbit, and another angle i_{Be} to the observer on Earth. The orbit in turn, is inclined at an angle i to the observer. The disk is oriented in such a way as to eclipse the pulsar, and a shock front forms from the stellar wind – pulsar wind interaction. The dashed portion of the orbit is behind the plane of the sky with S (the Be star) as the origin. P is the point of periastron, and the pulsar passes through the disk at points A and B.*

to form a bow shock and become cometary in shape, as in figure 2.2, and shock fronts form on both sides of the interface (Johnston et al. 1999). The size of this bubble is determined by the momentum flux balance between the Be star wind and relativistic pulsar wind.

In equations 1.6 and 1.7, $\beta = 2$ corresponds to a constant velocity and $\beta = 4$ corresponds to constant ram pressure. The polar wind velocity and density can be approximated by setting $\beta_w = 2$, and $v_{w0} \sim 1000$ km s^{-1}. For the disk, $\beta_d \lesssim 4$ and $v_{d0} \sim 5$ km s^{-1}. The number density of the disk wind at the star surface is $n_{d0} \sim 4 \times 10^{18}$ m^{-3}, and the surface number density of the polar wind is $n_{w0} \sim n_d/1000$ (Ball et al. 1999).

PSR B1259−63 shows only a very low level of X-ray flux. Almost immediately after the pulsar reaches apastron, the flux becomes measurable, and then increases by a factor of ~ 10 towards periastron (Cominsky, Roberts & Johnston 1994; Hirayama et al. 1996). Modelling suggests this is synchrotron radiation from relativistic pulsar wind leptons that are accelerated at the shock between the pulsar and Be winds (Kaspi et al. 1995; Tavani & Arons 1997).

2.2 Evolution of the system, past and future

If the supernova was symmetrical, the observed high eccentricity of the orbit, $e = 0.87$, requires the mass of the primary star (the one to become the pulsar) to be about $12 M_\odot$ (Johnston et al. 1996) before the explosion. Roche-lobe overflow would have occurred, so the companion gained

a few solar masses, enabling the system to stay together after the explosion. Before this evolution, the system was perhaps a $25 M_\odot$ star being orbited by the $5 M_\odot$ companion in a long period circular orbit. The heavy star evolved quicker, and the then lighter star is now the Be star.

Orbit shrinkage occurred during the Roche-lobe overflow, and the orbital period became about 50 days. After the explosion, a recoil velocity of 80 km s^{-1} was imparted on the system, consistent with the blueshift observed. The explosion also disrupted the orbit to what is seen today.

The Be star is likely to evolve before any other evolution in the system, such as the pulsar turning off, or the orbit circularising (Johnston et al. 1994). Roche-lobe overflow will not occur, unless the orbit spirals in significantly from tidal drag during the red-giant phase. If the overflow occurs, a HMXB will result. The system may separate after the second supernova, or it may remain, resembling PSR B1913+16 (Harrison & Tademaru 1975).

2.3 Previous observations and models

2.3.1 1994 periastron

At periastron (the closest approach of the two stars — epoch of periastron is denoted $\mathcal{T}$), the stars are separated by $25 R_c$ (Johnston et al. 1994), assuming the radius of the companion star is $6 R_\odot$. This distance is comparable to the radius of the Be disk, so the pulsar passes through the disk, possibly disturbing and warping it. During the 1994 passage (Johnston et al. 1996), the DM increased by up to $\sim$11 cm^{-3} pc before the eclipse. The radial power law (equation 1.6) applies with $\beta = 4.2$ and $n_0 = 4.5 \times 10^{18}$ m^{-3}. The DM first became affected by the wind at a distance of $\sim 150 R_c$ from the Be star. With a radial outflow of stellar wind at ~ 5 km s^{-1}, a mass loss of $5 \times 10^{-8} M_\odot$ yr^{-1} is expected. The disk electron temperature is around $\sim 10^4$ K (Melatos, Johnston & Melrose 1995), and its half-opening angle σ_d was thought to be $\sim 15°$, but has been revised to less than $10°$ (Johnston et al. 1999) from the 1997 data, and possibly as low as $5°$ (Ball et al. 1999).

The rotation measure of the pulsar was measured over the entire period, and varied by as much as -6650 rad m^{-2}, from the assumed galactic contribution. When combined with the DM measurement, the magnetic field (projected radially from the Earth), weighted as a function of electron number density over the line of sight can be obtained (equation 1.4). The pulsar acts as a probe to the disk since that is where most of the matter in the line of sight is, and when the RM was 6650 rad m^{-2} from the galactic value, the pulsar was $45 R_c$ from the companion, and the field strength was ~ 40 mG — representing the first direct measurement of field strength near a Be star (Johnston et al. 1996).

2.3.2 1997 periastron

Johnston et al. (1999) observed the 1997 periastron (light curve in figure 2.3a) and Ball et al. (1999) modelled the unpulsed radiation (figure 2.3b). From $\mathcal{T} - 20$ days to $\mathcal{T} + 16$ days, eclipse of the pulsar occurred — and the eclipse is attributed to free-free absorption in the Be disk. Unpulsed (referred to as continuum) flux begins at $\mathcal{T} - 22$ days and lasts until at least $\mathcal{T} + 100$ days. The spectral index (equation 3.2) of the continuum flux during this time (figure 2.4) is mostly -0.5 to -0.7 — implying synchrotron emission. Peaks at $\mathcal{T} - 10$ days and $\mathcal{T} + 20$ days are from non-relativistic Be disk or polar wind electrons that are accelerated in the shock(s) between the pulsar wind and the Be disk, however some radio continuum emission may be from the pulsar – Be wind interaction. The X-ray synchrotron emission is produced via different physics, and is thought to be caused by the interaction between the pulsar wind and Be star

a)   **b)**
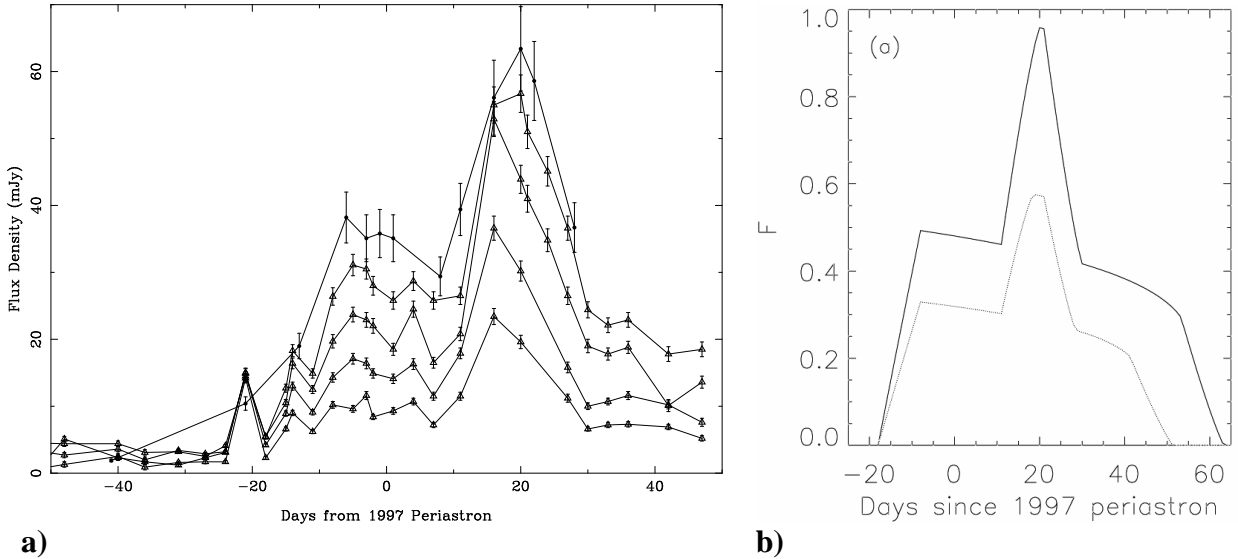
Figure 2.3: **a)** *Light curve at all observed frequencies, for the 1997 periastron (Johnston* et al. *1999). From top to bottom, the flux densities are at 0.84, 1.4, 2.5, 4.8 and 8.7 GHz. The 0.84 data has less data points (observations) as it was observed on a different telescope (MOST).*
b) *Model of the continuum (non-pulsed synchrotron) flux at an arbitrary frequency ν (solid line) and $\nu' = 1.44\nu$ (dashed line), demonstrating the changing spectral index (Ball* et al. *1999).*

outflow (Tavani, Arons & Kaspi 1994; Kaspi et al. 1995; Tavani & Arons 1997). The Be polar polar wind velocity is 2000 km s^{-1}, and it is this wind that causes most of the dispersion measure changes (Johnston et al. 2001).
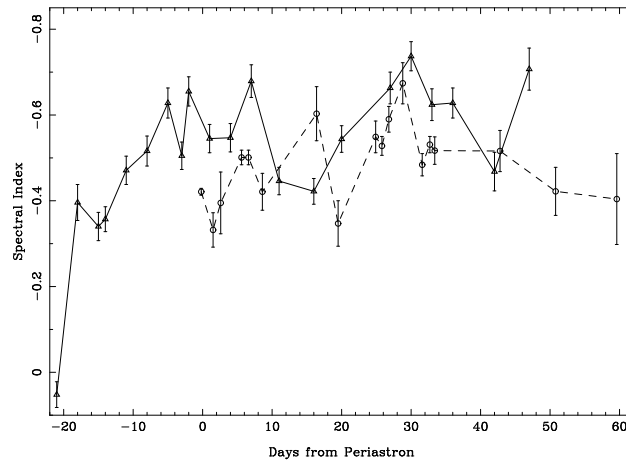
Figure 2.4: *The spectral indices (Johnston* et al. *1999) for both 1994 and 1997 periastra (dashed and solid lines, respectively).*

The model argues that the radiating electrons are accelerated in a time lasting longer than the two disk crossings, which are ~ 3 days long (implying a disk opening angle of $\sigma_d \sim 5°$). The electron population evolves through synchrotron losses. A fit of 10 days was obtained for the electron acceleration time, and this is the period of the initial rise time before periastron. The time constant of the gradual decay from the pre-periastron peak, which continues after the post-periastron peak, is dependent upon the strength of the magnetic field, and since the magnetic field is higher for the second peak, because the pulsar is closer to the Be star, it decays faster. The rise time of the post-periastron peak is defined by the synchrotron loss time, and is the same as its fall time, but is also fitted to be approximately the same as the rise time of the pre-periastron peak.

10

We are left with just the electrons from the first disk crossing, after $\mathcal{T} + 35$ days. There is a flat spectrum spike at the start that is possibly due to the pulsar wind splashing into the disk, but more importantly, the model makes a prediction that since the high energy electrons evolve quicker in time, a high frequency cutoff in the synchrotron spectrum (Melrose & McPhedran 1991) moves gradually to lower frequencies, and the light curve suddenly drops to zero with a frequency dependency, just after the last full spectrum data was obtained during 1997. Verification of this late-time behaviour for the 2000 periastron is one of the key aims of the project.

2.4   This Project

PSR B1259$-$63/SS2883 was observed using Australia Telescope Compact Array (ATCA, near Narrabri) over the period from $\mathcal{T} - 46$ to $\mathcal{T} + 113$ ($\mathcal{T} + x$ denotes time since periastron in days, where periastron was 17 October 2000).

In 2000, PSR B1259$-$63 underwent its last periastron, and preliminary analysis suggested the continuum (unpulsed) flux from the pulsar was different from the 1997 periastron. There was also some hint of a very high rotation measure, suggesting a high magnetic field in the vicinity of the Be star.

A new MIRIAD routine not available in previous years, and the new correlator at the ATCA that can observe in pulsar binning mode with 16 time bins instead of 8 (for the 1997 observation) or no bins (1994) have been utilised in this project, to separate the effect of the continuum and pulsed fluxes, and in combination with more detailed observing, we should be able to improve upon models presented in former periastra.

In this project, our objectives are:

- To produce a light curve for both the continuum and unpulsed flux densities at all frequencies and all observing times, and compare with the observations and model from 1997, and in particular, compare with the predicted late time behaviour ($\gtrsim \mathcal{T} + 60$).

- To obtain spectral indices for continuum flux for as many days as possible, and compare with the Ball et. al. (1999) model.

- To obtain the RM of the pulsar at different epochs to probe the magnetic fields near the Be star.

- To check the rise, sustain and fall times of the continuum flux from the system, and compare with the Ball et. al. (1999) model (figure 2.3b).

- To explain the physics behind any differences from the model, such as disk warpages, disk orientation changes, density structure variations in the various winds, or growth or decay of the disk.

Chapter 3

Observing, data reduction and analysis

3.1 Observations

Observations were made at the Australia Telescope Compact Array (ATCA) in Narrabri. It is possible to observe at two frequencies simultaneously with full polarization information, with a nominal bandwidth of 128 MHz, and nominal spectral resolution of 4 MHz (i.e. 32 channels). However, adjacent frequency channels are not completely independent, and after removal of the band edges, we are left with 13 channels and a resolution of 8 MHz. The ATCA is capable of splitting each correlator cycle into bins corresponding to different phases of a pulsar's period, and the pulse profile can be split into 8, 16 or 32 bins.

Our observations were made at 1384 and 2496 MHz simultaneously, alternating with 4800 and 8640 MHz, and the observations were folded synchronously with the pulsar period of 47.8 ms, dividing the pulse profile into 16 time bins. An example pulse profile appears in figure 3.2. Full Stokes parameters (see table 3.1) were recorded.

Stokes parameter	Definition for linear receiver feeds
I	$\langle E_x^2 \rangle + \langle E_y^2 \rangle$
Q	$\langle E_x^2 \rangle - \langle E_y^2 \rangle$
U	$2\langle E_x \rangle \langle E_y \rangle \cos \delta$
V	$2\langle E_x E_y \rangle \sin \delta$

Table 3.1: *Definitions of the 4 Stokes parameters in terms of the orthogonal electric fields (Turlo et al. 1985).*

One of the ATCA primary flux calibrators, $0823-500$ or $1934-638$, was observed once during each session for ~ 5 mins to fix the flux densities of the pulsar. Each pair of bands were switched every ~ 20 mins, with an observation of the secondary phase calibrator ($1251-713$) for ~ 3 mins leading each integration, where the phase calibrator compensates for the changing propagation within the Earth's ionosphere.

Thirty observations between $\mathcal{T} - 46$ and $\mathcal{T} + 113$ were made using various ATCA configurations. The observing times were from 2 to 8 hours long, with most being 4 hours, and the observations are detailed in table 3.2.

The observations with "*" next to them in table 3.2 were either too short to be of any use, or didn't have proper time-bin observing during all of or part of the observation. Since the pulsar is a single point source (although it has to be resolved from a nearby source), any telescope array size was useful, although a 6km array was preferred, to minimise noise from local and solar interference, since these affect the shorter baselines. The shortest array used was a 750m

Observation start time (UT)	Length	Array config	Observation start time (UT)	Length	Array config
Sep 01.00	4h	6A	Oct 26.97	4h	6C
Sep 08.99*	1h	6A	Oct 30.71	4h	6C
Sep 15.05	4h	6A	Nov 04.67*	4h	6C
Sep 23.05	4h	6A	Nov 04.85	8h	6C
Sep 25.05	4h	6A	Nov 07.79	2h	6C
Sep 27.06	4h	6A	Nov 10.84	4h	6C
Sep 29.00	4h	6A	Nov 15.93	4h	1.5B
Sep 30.88	4h	6A	Nov 20.72	4h	1.5B
Oct 02.74	4h	6A	Nov 26.72	4h	1.5B
Oct 05.22	4h	6A	Dec 08.84*	4h	1.5B
Oct 06.88	4h	6A	Dec 11.72	4h	1.5B
Oct 11.05	4h	6A	Dec 19.86	4h	1.5C
Oct 14.79	4h	6A	Dec 26.79	5h	750C
Oct 18.89	4h	6C	Jan 08.49	5.5h	750C
Oct 23.01	4h	6C	Feb 07.72	4h	6C

Table 3.2: *Date, length of observation in hours, and array configuration for all observations of PSR B1259−63/SS2883 during the 2000 periastron. Entries with "*" next to them have not been analysed yet because of difficulties. The longest baseline in the 750C array is usually 750 metres, and 1.5 kms for the 1.5B and 1.5C arrays, and 6 kms for the 6A and 6C arrays, but we always make use of the 6th antennae that is between 3 and 6 kms away from the others.*

array (with the 6km antenna still included to bring the array back up to a 3–6 km array) on two occasions towards the end of the observing period. The shorter baselines in these arrays typically were completely flagged out (or rejected) at the two lower frequencies, because of excessive interference.

3.2 Data reduction

3.2.1 Overview

All data reduction was performed using the MIRIAD data reduction package. A large number of scripts (programs that ran and then interpreted the results from the MIRIAD tasks) were produced to semi-automate the large task of reducing thirty different observations. A description of these scripts can be found in appendix A, and a flowchart in figure 3.1. The first thing we did that differed from previous analyses was to subtract the continuum flux density from each time bin equally, allowing us to separate the total flux into continuum flux and on-pulse flux.

We form images from the pulsar on-pulse flux (which contains no other sources in the field, since nothing else fluctuates at the same frequency PSR B1259−63 does). We also form a total flux image (an image of the system with nothing subtracted), and deduce the continuum flux by subtracting the pulsed flux from the total flux.

A rotation measure was obtained for each frequency that it could be measured, and these were averaged. The RM varied on a time-scale of smaller than an hour, so in several sessions, the observations were split into blocks of about half an hour. Total flux density (Stokes I) and circularly polarized flux density (Stokes V) were obtained, with a light curve and spectral index being derived from the total flux. In the following sections, we discuss the reduction in more detail.

3.2.2 Calibration

The UV data (raw data in the Fourier plane) is automatically flagged to remove bad data, and calibrated by the DO_CAL script, which makes use of TVCLIP to flag all data points more than 6 times the average absolute deviation from the mean flux density (Sault & Killeen 1998). The script then calibrates the data using the standard method detailed in Sault & Killeen (1998).

The flux densities of the primary calibrator $0823-500$ are fixed at 5.5, 5.6, 3.1 and 1.4 Jy (where a Jansky is a unit of flux density defined by $1\,\mathrm{Jy} = 10^{-26}\,\mathrm{Wm^{-2}Hz^{-1}}$), and those of $1934-638$ are 14.9, 11.6, 5.8 and 2.8 Jy, for the 4 observing frequencies respectively (Johnston et al. 1999). The flux density of $1251-713$ is ~ 1 Jy at all frequencies.

We calibrate the antenna gains, bandpass function and delays using MFCAL, and leakages between the polarizations using GPCAL, for the primary calibrator, assuming no linear polarization. We then calibrate the secondary calibrator in the same way, solving for a non-zero linear polarization, and additionally setting the calibrator's absolute flux scale from the primary calibrator using GPBOOT. Once the gains, phases and leakages for the antennae are fully calibrated for the secondary calibrator, we propagate the gain tables to the source using GPCOPY.

Figure 3.1: *Outline of the data reduction and analysis process.*

3.2.3 Imaging

Although it is possible to directly measure the flux density of the pulsar using UVFLUX, another source is nearby that will contribute flux to the measurement through its sidelobes, and so it is usually desirable to image the pulsar (with INVERT), and remove the sidelobes from the image (or "clean" the image using CLEAN and RESTOR). These tasks are handled automatically by the DO_IMAGE script, which chooses appropriate image sizes and resolutions for each frequency, and specifies that the inversion is performed using a robust weighting scheme and taking into account the system temperature when weighting visibilities[1].

To speed up the imaging process, we first average the bin-mode data using the DO_AVER script, which directs UVAVER to average each bin from the pulse profile together. INVERT images just the Stokes I data, by performing a Fast Fourier Transform on the UV data, and generates a dirty image. CLEAN removes the side lobes iteratively by generating delta functions corresponding to point sources (clean components), and removing them from the UV data, until there is just a "residual map" left. The clean components are added to generate a "clean map" and the RESTOR program adds the residual map back to the clean map, convolving it with the primary beam of the dirty image to produce the final image. The final image has all sidelobes removed, if the data is well flagged, and the flux density is in units of Jy per beam, so the pulsar's flux can be directly measured from it.
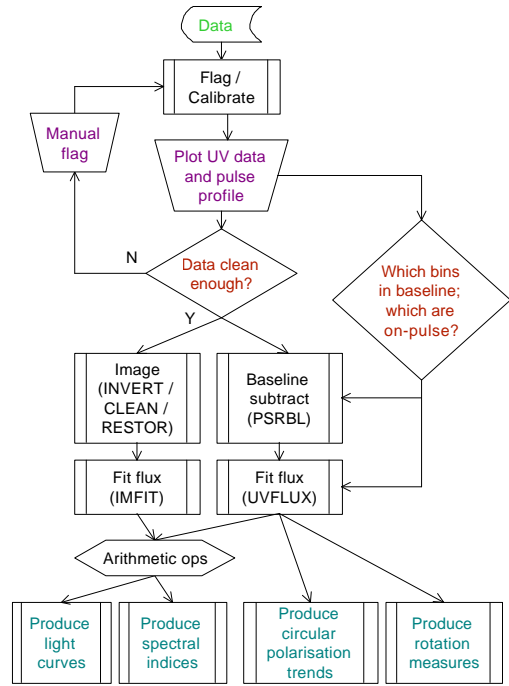
---

[1]The relevant options supplied to INVERT are "options=...,systemp" and "robust=0.5"

3.2.4 Pulsar data

The UV time binned data is first corrected for dispersion using DO_FIX, otherwise the pulses smear out for the lower frequencies, since the time delay across the frequency band is a significant fraction of the pulse period. We assume a constant DM of 146.7 cm^{-3}pc, which is accurate enough to de-disperse the profile completely.

We wish to be able to model the continuum emission from the pulsar separately from the pulsed emission, since the changes come from different physics. In the last analyses performed (Johnston et al. 1999), this was not done for all days, as the pulse profiles were only split into 8 time bins, rather than 16, and there was no MIRIAD task that was capable of doing the splitting.

We have to first look at the pulse profile using PSRPLT to see which time-bins are part of the baseline, then give these bins to the DO_PSRBL script. The new PSRBL task in MIRIAD is utilised by DO_PSRBL, and takes care of subtracting the average of the baseline (off-pulse) bins from the UV data, for all Stokes parameters for each integration, and for each frequency channel. The only flux left in the UV data is the pulsar flux — all sources that are not synchronised with the pulsar period are subtracted, since they will contribute equally to all the bins in the UV data.

We then look at the new pulse profile using PSRPLT, and decide which bins ought to be used in the RM calculations and which bins are included in the various on-pulse flux measurements (the more bins included, the higher the signal for flux measurements, but the lower the accuracy of RM measurements, since the position angle changes across the pulse profile). An example pulse profile and bin selections appear in figure 3.2.

a)   b)
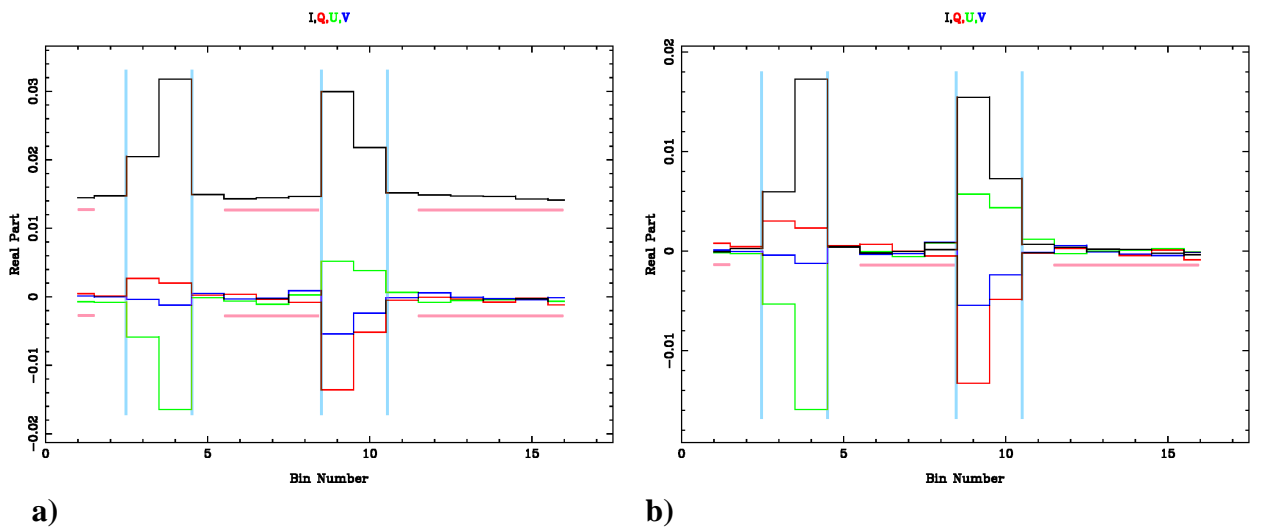
Figure 3.2: *A pulse profile (Nov20 2000, 4800MHz, all time and channels) demonstrating the Stokes parameters, and how the baseline is selected.*
a) *The bins inside the vertical blue lines are the bins counted as being on-pulse (for the percentage circular polarization measurements — the RM measurements typically used just the highest bins from each pulse component).*
b) *The bins associated with the horizontal red lines are the bins selected as part of the baseline, and are subtracted to give the second figure. By definition, all the Stokes parameters in these bins in the baseline subtracted profile average to 0. It is clear that the second component has a lot more circular polarization than the first, and the linear polarization is both a high percentage of the total flux, and show 90° difference between the components.*

15

3.2.5 Flux density measurement

DO_IMFIT

DO_IMFIT is used to fit a point source flux distribution to the pulsar (either on-pulse or the combined continuum and pulsar total fluxes), in the clean image. This script utilises IMFIT to fit to a point source fixed at a certain position relative to the observing centre.

The fitting is done with care, making sure the values are sane, by checking the image using a visualization package such as KVIEW.

DO_UVFLUX

The DO_UVFLUX script (and variants) measures the flux density of a point source with a given position relative to the observing centre, directly from the UV data. In normal observing, this flux may be biased from other sources, since the sidelobes of those sources will not be removed from the data, however the baseline subtracted UV data contains only the pulsar — all other flux has been subtracted from the UV plane, since no other flux will be synchronous with the pulsar period. This means there will not be any side-lobe overflow onto the pulsar, and we can use UVFLUX with high accuracy.

UVFLUX is more susceptible to incomplete flagging, or noise in general, and underestimates the flux if there are phase problems. However, IMFIT can not be used for low flux data (for on-pulse data, when the pulsar is partially eclipsed) at all, because of cleaning problems. When the pulsar is completely eclipsed, we do not worry about baseline subtraction and UVFLUX, so less care needs to be taken with flagging.

The various DO_UVFLUX scripts are used for the on-pulse (base-line subtracted) data to measure the flux density for the 4 Stokes parameters as appropriate. For RM measurements, they may be given channel ranges to work on. They may also be given bin numbers if it is desired to measure the fluxes in the two pulse components individually. The flux can be measured for the full continuum and pulsed data, but this is only used to check against the fluxes given by DO_IMAGE and DO_IMFIT. If the errors are very high compared to the theoretically expected noise, or the results from DO_UVFLUX and DO_IMFIT differ too much, flagging is reperformed manually, and the entire process restarted. Fortunately, most of the work in getting to this stage was in flagging and choosing bins (which remain constant, independent of flagging), so the scripts can be rerun many times with ease.

By subtracting the on-pulse flux obtained using DO_UVFLUX from the combined flux obtained using DO_IMFIT, we can deduce the flux contributed purely from the continuum synchrotron radiation.

Once many observing sessions have been reduced, we can then form separate light curves from the 3 sets of fluxes — continuum, pulsar, and the full flux. The full flux data is directly comparable to the light curve produced for 1997 shown in figure 2.3a.

3.3 Analysis

3.3.1 Obtaining a light curve

One of the key predictions from the 1997 observations of PSR B1259−63/SS2883, is the model light curve in figure 2.3b. We aim to verify the behaviour, and see whether the new data follows the model. We use a combination of DO_UVFLUX (for on-pulse flux) and DO_IMFIT (for continuum and pulsed flux) in the GENERATEFLUXERRTABLE.PL script (who's main job is to handle

the parsing of the fitting output), which then outputs to GNUPLOT routines LIGHTCURVES-CONT.GNUPLOT, LIGHTCURVESCONT+PSR.GNUPLOT and LIGHTCURVESPSR.GNUPLOT. These GNUPLOT routines output the light curve for all frequencies, of the on-pulse flux, the pure continuum flux, and total flux.

The light curve for the 1997 total flux data is shown using the LIGHTCURVES1997.GNUPLOT script, and the corresponding 2000 data is shown using LIGHTCURVES1997.GNUPLOT.

3.3.2   Circular polarization

Circularly polarized flux should not be depolarized by the plasma around the star or the interstellar medium, and so we can verify linear-polarization measurements by making sure the circular polarization (Stokes V) as a fraction of the total flux density (Stokes I) is constant within the error bars over the full observing time periods. If not, the reliability of our RM measurements later may be cast in doubt.

We use GENERATECIRCERRORTABLE.PL to look at the circular polarization in the pulse components separately, and then over the complete pulse profile. GENERATECIRCERRORTABLE.PL makes use of the DO_UVFLUX and DO_UVFLUXINDIVPULSES scripts (using UV data, since we are only dealing with pulsar flux). We use the CIRC0.GNUPLOT (for the whole pulse profile), CIRC1.GNUPLOT and CIRC2.GNUPLOT (for first and second components, respectively) scripts to plot the circular polarizations.

It is known from previous observations that the first pulse component has a very small circular polarization, whereas the second component has a polarization in the tens of percentage range (figure 2.1), and we can verify this behaviour again.

3.3.3   Obtaining the RM

The RM measurements are obtained for the on-pulse data, by dividing each receiver's bandwidth into ~ 6 sets of channels, and measuring the position angle in each, and seeing how it varies. This task is handled by the PLOTRM.PL script, which uses DO_UVFLUXRM to get the flux densities, errors, and number of visibilities for each time, bin and frequency selection relevant. The position angle is given by (Turlo et al. 1985):

$$\phi_\nu = 0.5 \times \tan^{-1}(U_\nu/Q_\nu) \qquad (3.1)$$

and can be related to the RM by equation 1.5.

The RM is obtained by measuring Q and U, and hence ϕ_ν, for each pulse component separately. The position angles are plotted against ν^{-2} in the ATCARM program, which then uses the Numerical Recipes routine "linfit" and fits for a simple straight line with errors, to obtain the RM. The RM's for the two components are computed as a consistency check. When the signal to noise is sufficiently high, we can separate the observation into multiple time intervals, and resolve RM changes with small time scales. However, when it is too low (whenever the pulses are being partially scattered) the entire observation must be used to get enough signal, and we can not resolve changes in RM with time. During most of the periastron, the pulses are completely eclipsed, in which case we can't obtain measurements for the RM.

Losses in sensitivity of Q and U lead to increases in the error of ϕ. The position angle is known to sweep over a small range over the pulse profile (figure 2.1), and is occasionally quite obvious just by looking at the Q and U values within a pulse component. The sweeping will cause a depolarization, which decreases the Q and U flux densities, and hence increases the errors in ϕ. Sometimes the errors can be improved by taking a single time-bin instead of multiple bins, despite there being less UV data present. Another loss can be caused by ϕ rotating too quickly

across a single frequency channel. This can occur in the case of extremely high RM's, but can be worked around by moving to the next higher frequency band. At the lowest frequencies, for times when the RM is high, the pulses appear completely depolarized even within one frequency channel, with Q and U both being 0 within the errors, and hence ϕ is meaningless in these situations.

3.3.4   Spectral indices

The flux density of the continuum or pulsed flux at a given frequency ν, is given approximately by a power law, with

$$F_\nu = C\nu^{+\alpha} \tag{3.2}$$

where α denotes the spectral index. We obtain the spectral indices for each session for the pulsed data only, the continuum data only, and the full data, and compare the trend over the 160 days with that in the 1997 data (Johnston et al. 1999).

We use the CALCSI.PL script to calculate α for each observing session, by doing a simple linear fit in log-log space for the fluxes as a function of frequency. The GNUPLOT scripts CONTSIS.GNUPLOT and PSRSIS.GNUPLOT then give α as a function of epoch.

3.3.5   Error analysis

Light curve

The full PSR B1259−63/SS2883 flux density is obtained using IMFIT, and IMFIT returns the residual RMS noise in the image. Since our source is a point source, this RMS noise should be the same as the expected error of the source. Hence we use this error in the light curve.

When looking at the pulsar only, we expect the error (as well as the flux) to go down, since there is nothing else in the field who's sidelobes would interfere with the pulsar's flux. However, deciding which bins contain pulsar flux is sometimes difficult, especially when there is some scatter broadening (light rays take different paths through the dispersive medium, and so incur different delays). In these cases, the splitting of pulsar and continuum fluxes will be erroneous, and the pulsar flux will be underestimated since some pulsar flux will spill over evenly into the baseline bins, and hence the continuum flux overestimated. This error seems to be unquantifiable.

Since we use UVFLUX to obtain the flux density, we use UVFLUX's "RMS scatter" value, which measures the scatter around the mean flux, and is the same as the theoretical RMS only for well calibrated data (Sault & Killeen 1998), in the calculation of our error. The RMS is given per visibility, so we divide by the square root of the number of correlations to give the error.

Circular polarization

The fractional circular polarization is given in terms of I and V, which have equal errors associated with them. Hence the error is

$$\Delta(V/I) = \frac{V}{I}\left[\left(\frac{\Delta V}{V}\right)^2 + \left(\frac{\Delta I}{I}\right)^2\right] = \frac{\Delta}{I}\frac{\Delta}{V}\left[1 + \left(\frac{V}{I}\right)^2\right] \tag{3.3}$$

where Δ is the RMS in both V and I. The same calculation is made when using DO_UVFLUX-INDIVPULSES for the pulse components — where the script is given a bin selection to work on, and GENERATECIRCTABLE.PL calculates the error for both V and I in the normal way with the reduced number of visibilities. Because there is more flux available on average in the pulses than over the entire time period, the fractional error in flux when including only the on-pulse bins is

smaller, and goes in first order as $\sqrt{n/w}$ for $n > w$ where n is the number of bins counted, and w is how wide the pulse component is. Hence the error in V/I can be seen from equation 3.3 to go approximately as n/w.

RM

The RM error calculations proceed by gathering the number of visibilities and RMS scatter from DO_UVFLUXRM for each block of data we are interested in. The error for the block is then calculated as in the above paragraphs. The error in ϕ is given by (Turlo et al. 1985):

$$
\begin{aligned}
\Delta\phi &= \frac{0.5}{Q^2 + U^2} \left[(Q\Delta U)^2 + (U\Delta Q)^2 \right]^{1/2} \\
&= \frac{0.5\Delta}{(Q^2 + U^2)^{1/2}} = \frac{0.5\Delta}{L} \qquad (\text{assuming } \Delta U = \Delta Q = \Delta) \qquad (3.4)
\end{aligned}
$$

where L is the linear polarization, with a small modification for practical calculations — subtracting a bias $B = 0.822\Delta$ from the quantity in the denominator in equation 3.4 and taking the absolute value of the result to give equation C.2, otherwise $Q^2 + U^2$ are biased positively by their errors (see appendix C).

The angles and their errors for each pulse component are fed through a "linfit" numerical recipes routine that calculates the RM and error, from a simple linear fit.

Spectral Indices

It would be ideal to fit the data for equation 3.2 using the "Marquardt-Levenberg" algorithm which takes into account the errors on the fluxes properly, even though they aren't symmetrical in log-space. However, since there are only 4 frequencies to fit for, this algorithm breaks down, and we have to resort to a simple linear fit that takes into account the errors only approximately, by treating them as symmetrical in log space. We then use normal χ^2 fitting to obtain errors for the spectral index for each session.

Chapter 4

Results — Light Curve

In this chapter, I will describe the flux densities of the combined pulsar and continuum source, and separated pulsar and continuum flux densities for each of the 30 observations at the four frequencies, including a full treatment of the errors. Chapter 5 details the polarization measurements and errors.

a) *Dirty map of full data.* **b)** *Cleaned image of full data.*

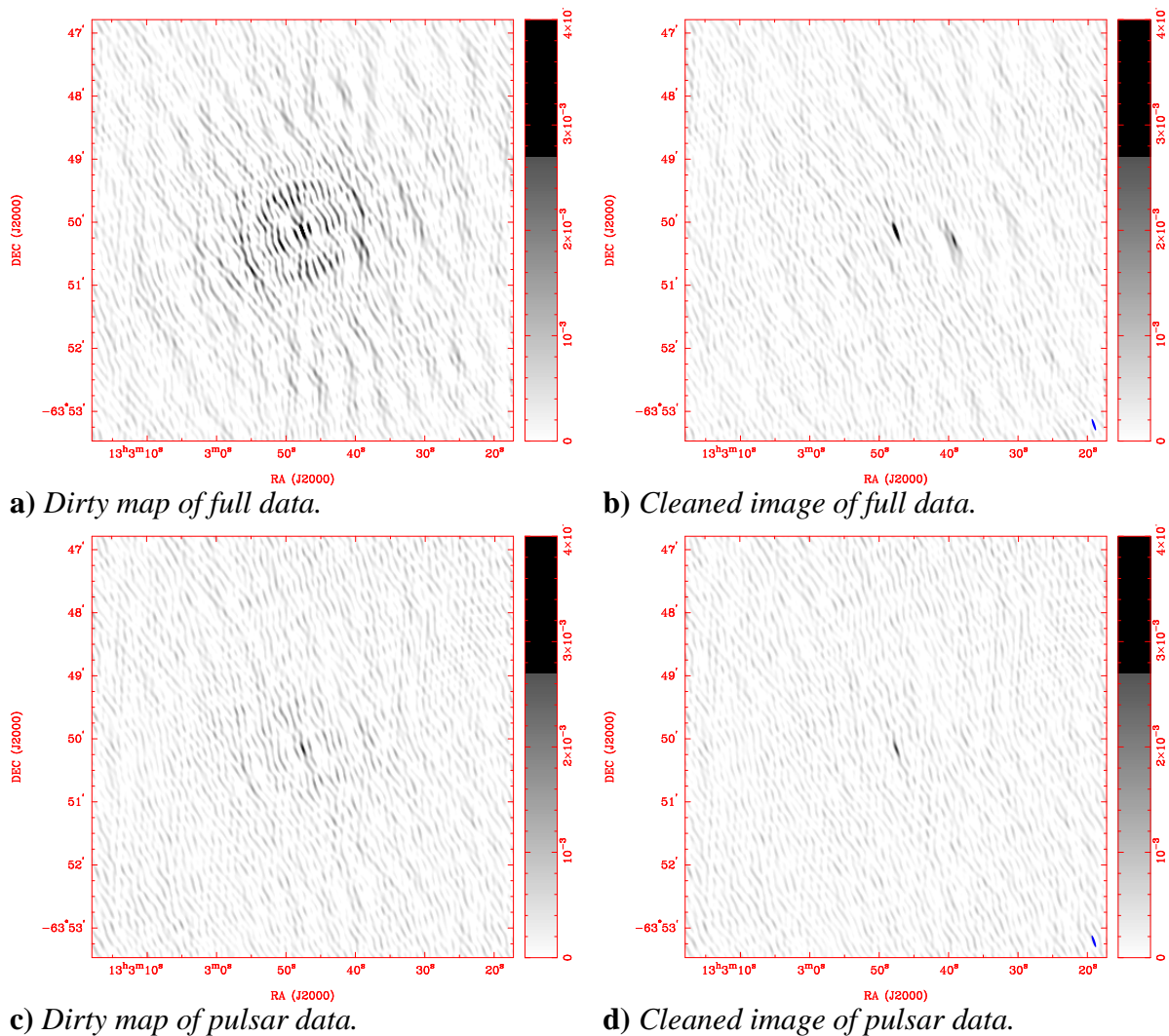**c)** *Dirty map of pulsar data.* **d)** *Cleaned image of pulsar data.*

Figure 4.1: *Images from the December 19, 2000 data at 2496 MHz. Stokes I, range 0 to 4 mJy (Total flux density for this day was 10.3 mJy, and the pulsar flux density was 3.6 mJy). Beam sizes for cleaned maps are shown in bottom right corner of images.*

Typical clean and dirty images at 2496 MHz are shown in figure 4.1, for data from the December 19, 2000 observation. The top row shows images made using the original data, and the bottom row shows images using the baseline subtracted data, containing only the pulsar flux (a demonstration of the baseline subtraction process is in figure 3.2). The left images are the dirty maps, and the right images are cleaned. The source in the middle of the field is the pulsar system, and to the west is a resolved extragalactic source with peak flux density ~ 3.5 mJy and integrated flux density ~ 5 mJy at this frequency.

Figure 4.1a demonstrates the importance of imaging and cleaning the non baseline subtracted data — it is obvious that the flux measurements of the non-baseline subtracted source in the dirty map (effectively what UVFLUX samples) are going to be biased from the sidelobes of the nearby resolved extragalactic source, and the bias is only removed in figure 4.1b upon cleaning. The baseline subtracted data in figure 4.1c does not have this problem, and it seen that there are no other sources left in the field in the cleaned image in figure 4.1d, as expected.

The flux densities from the observations listed in table 3.2 appear in table 4.1. The first column shows the date of the observation, as well as the time from periastron in days. The second column shows the frequency — most observations were at all 4 frequencies, but one was allocated on a "target of opportunity" basis, and only used the lower frequencies. The flux density of the pulsar, as calculated by UVFLUX, is given in column 3, for when significant pulsed flux is detected. The pulsar error in column 4 is nominally the error calculated from the RMS scatter, as described in section 3.3.5. However, when the imaginary component of the flux density calculated in UVFLUX is more than 4 times this, the atmospheric phase stability was very bad and the quality of the data is questionable, and the new error is shown in brackets. Column 5 gives the combined pulsar and continuum flux density, as measured by IMFIT, and the error in column 6 is taken from the image RMS residual in IMFIT.

Light curves are produced from the data in table 4.1, and the light curve of the combined pulsar and continuum flux densities appear in fig 4.2a, pulsar flux in figure 4.2c, and continuum flux (the pulsar flux subtracted from the combined flux) in figure 4.2b. A comparison of the full light curves of 1997 and 2000 appear in figure 4.3. In all cases, colour differentiates the frequencies. The continuum and combined light curves are interpolated between observations, because they are assumed not to vary significantly on time-scales of a day, but the pulsar flux is assumed to be highly variable on the time-scale of hours because of scintillation, so are plotted as discrete points. Error bars are plotted as appropriate for the type of flux measurements — errors from UVFLUX for the pulsar data, and IMFIT for the combined pulsar and continuum data.

The plots in the comparison of the 1997 and 2000 data are plotted on the same scale, concentrating on a subset of all the 2000 data to highlight the interesting events, and lines at $\mathcal{T} \pm 20$ are drawn to ease comparisons, since this is roughly where the pulsar abruptly becomes both non-detectable and then detectable, and the continuum flux starts to rise or peak. A line is also drawn at the point of periastron to enable easy comparisons.

4.1 Pulsar

4.1.1 Eclipse mechanisms

Material from the Be star surrounds the pulsar, and contributes to scattering of the light rays from the pulsar. A ray that is emitted from the pulsar and arrives at the observer unscattered, has a shorter path-length than a ray that scatters off the material. The probability of a certain scattering angle and hence delay is approximated exponentially, and so the time of arrival of light rays from a fixed phase of the pulse profile will have an exponential tail with a time constant τ_s which is strongly frequency dependent, $\tau_s \propto \nu^{-4.4}$ (Cordes, Weisberg & Boriakoff 1985). In this way, the

Table 4.1 (left panel)

Day (+𝒯)	Freq (MHz)	Psr Flux	Psr Error	Psr + Cont Flux	Psr + Cont Error
sep01 (−46.4)	1384	5.36	0.12	8.00	0.73
	2496	4.77	0.19	4.61	0.20
	4800	2.75	0.10	2.76	0.18
	8640	1.76	0.08	1.81	0.16
sep15 (−32.4)	1384	—	—	3.93	0.65
	2496	2.47	0.21	5.00	0.43
	4800	2.27	**0.08 (1.28)**	2.22	0.48
	8640	0.61	**0.08 (0.61)**	0.78	0.32
sep23 (−24.4)	1384	—	—	1.64	0.37
	2496	—	—	3.34	0.33
	4800	2.15	0.17	2.28	0.39
	8640	0.61	0.09	0.64	0.19
sep25 (−22.4)	1384	—	—	3.78	0.56
	2496	1.38	0.20	4.29	0.43
	4800	1.70	**0.10 (0.61)**	1.70	0.30
	8640	1.10	**0.06 (0.67)**	1.13	0.31
sep27 (−20.4)	1384	—	—	2.03	0.29
	2496	—	—	1.62	0.25
	4800	0.60	0.10	1.43	0.34
	8640	0.44	0.09	0.65	0.25
sep29 (−18.4)	1384	0.29	0.13	4.73	0.64
	2496	—	—	5.36	0.34
	4800	0.57	0.14	3.26	0.40
	8640	0.22	0.09	1.58	0.40
sep30 (−16.5)	1384	—	—	6.44	1.06
	2496	—	—	6.86	0.31
	4800	—	—	4.62	0.38
	8640	—	—	2.86	0.42
oct02 (−14.7)	1384	—	—	17.60	1.91
	2496	—	—	13.28	1.29
	4800	—	—	9.17	2.41
	8640	—	—	3.18	1.85
oct05 (−12.2)	1384	—	—	27.39	2.62
	2496	—	—	23.27	1.57
	4800	—	—	12.06	3.71
	8640	—	—	3.09	2.20
oct06 (−10.5)	1384	0.51	0.16	33.37	1.68
	2496	—	—	29.61	0.78
	4800	—	—	21.95	1.16
	8640	—	—	13.68	1.11
oct11 (−6.4)	1384	—	—	39.64	2.91
	2496	—	—	29.83	2.01
	4800	—	—	13.93	3.33
	8640	0.22	0.09	3.27	2.05
oct14 (−2.6)	1384	—	—	29.16	1.70
	2496	—	—	23.70	0.84
	4800	—	—	16.17	1.97
	8640	—	—	9.18	1.98
oct18 (1.5)	1384	0.18	0.06	21.50	1.59
	2496	—	—	17.36	0.54
	4800	—	—	11.75	0.99
	8640	—	—	7.85	0.99
oct23 (5.6)	1384	—	—	21.72	1.24
	2496	—	—	16.93	1.07
	4800	—	—	10.15	2.52
	8640	—	—	3.70	2.21

Table 4.1 (right panel)

| Day (+𝒯)	Freq (MHz)	Psr Flux	Psr Error	Psr + Cont Flux	Psr + Cont Error
oct26 (9.6)	1384	0.35	0.13	22.57	1.62
	2496	—	—	15.88	1.19
	4800	0.22	0.08	6.79	1.54
	8640	0.18	0.08	1.22	0.50
oct30 (13.3)	1384	—	—	22.55	2.17
	2496	—	—	17.50	1.07
	4800	—	—	12.35	1.39
	8640	—	—	6.13	1.59
nov04 (18.5)	1384	0.12	0.05	29.88	1.46
	2496	0.29	0.08	23.22	0.92
	4800	0.39	0.06	11.02	1.42
	8640	0.36	0.05	2.46	0.76
nov07 (21.3)	1384	1.64	0.12	35.66	2.54
	2496	3.31	0.21	34.65	1.32
nov10 (24.4)	1384	2.97	0.17	36.95	2.27
	2496	5.12	**0.18 (1.03)**	34.60	1.46
	4800	4.33	0.18	22.95	2.01
	8640	1.59	**0.10 (0.58)**	13.40	1.55
nov15 (29.5)	1384	3.75	0.18	32.04	3.15
	2496	3.08	0.12	24.62	1.15
	4800	1.89	**0.06 (0.27)**	13.81	1.86
	8640	1.48	0.13	7.06	1.72
nov20 (34.3)	1384	3.33	0.13	26.69	2.70
	2496	3.61	0.17	23.61	0.80
	4800	2.94	0.09	17.27	1.06
	8640	0.86	0.08	9.62	0.99
nov26 (40.3)	1384	3.69	0.11	20.73	1.73
	2496	3.83	0.17	18.92	0.64
	4800	1.63	0.08	11.06	0.77
	8640	1.60	**0.08 (0.45)**	6.88	0.85
dec11 (55.3)	1384	4.05	0.15	15.47	1.72
	2496	3.56	0.19	11.70	0.38
	4800	1.11	0.12	5.43	0.32
	8640	1.65	0.10	3.80	0.33
dec19 (63.4)	1384	4.41	0.20	15.58	1.62
	2496	3.64	0.20	10.30	0.71
	4800	2.38	**0.06 (0.49)**	5.07	1.35
	8640	0.57	**0.06 (0.27)**	1.39	0.61
dec26 (70.4)	1384	5.09	0.18	10.25	1.84
	2496	4.11	0.12	7.47	0.55
	4800	1.92	0.08	5.19	0.55
	8640	1.07	0.06	0.75	0.41
jan08 (83.1)	1384	5.28	**0.20 (1.14)**	13.52	3.46
	2496	4.76	**0.16 (0.84)**	10.38	0.60
	4800	1.85	0.09	5.09	0.41
	8640	0.48	0.06	2.56	0.38
feb07 (113.3)	1384	3.60	**0.15 (0.99)**	10.85	0.86
	2496	3.39	**0.13 (1.24)**	7.97	0.63
	4800	3.87	**0.09 (2.94)**	6.46	2.08
	8640	0.74	**0.11 (1.35)**	2.19	1.31

Table 4.1: *Flux densities for both pulsar only, and continuum and pulsar. Pulsar flux densities are omitted when no significant pulsed flux was detected. Flux densities and errors for continuum and pulsar are from* IMFIT. *Flux densities and errors for pulsar only are from* UVFLUX.

pulses become scatter broadened. The closer the pulsar is to the Be star, the higher the density of material (see, for example, the density of the Be disk, equation 1.6) and the more likely rays are going to be scattered, lengthening the tail. If τ_s at a certain frequency is much greater than the time between the two pulse components, we can not expect to be able to detect the pulses.

The material along the line of sight can also attenuate the pulsar flux through free-free absorption. The optical depth can be approximated by

$$\tau = 8.2 \times 10^{-2} T^{-1.35} \nu^{-2.1} \int_{\mathrm{LOS}} n_e^2 \, \mathrm{d}l \qquad (4.1)$$

where the integral over LOS denotes the line of sight to the pulsar and T is the temperature in Kelvin, ν the observing frequency in GHz, and $n_e(l)$ the free electron density along the line of sight. The electron temperature in the wind is $\sim 10^4$ K (Waters 1986), and when the pulsar enters the disk, the extremely high n_e implies an optical depth $\gtrsim 10^5$ and we conclude that free-free absorption is a very important eclipse mechanism between $\sim \mathcal{T} - 20$ and $\sim \mathcal{T} + 20$ (Johnston et al. 1996; Johnston et al. 1999).
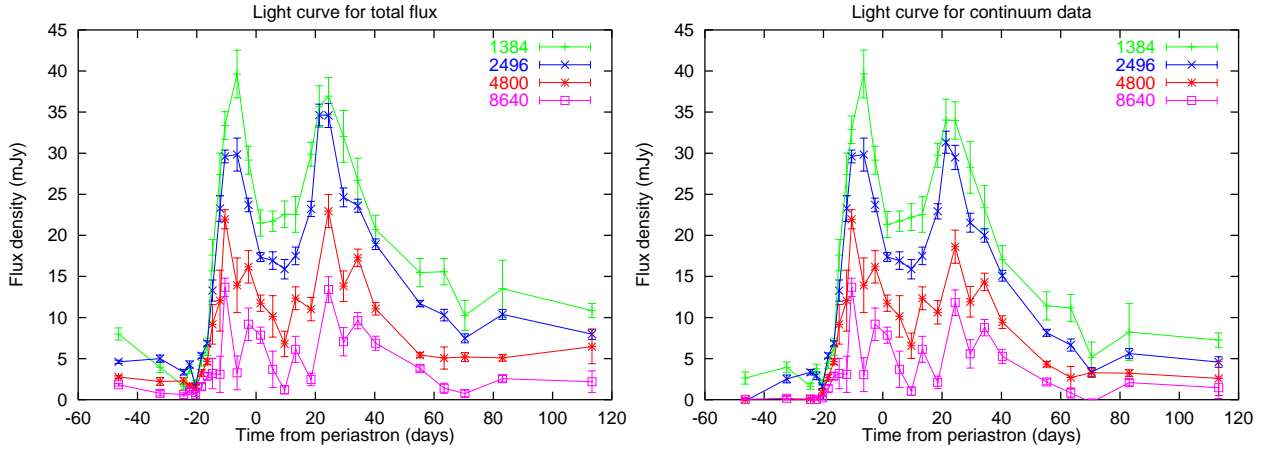
a) *The combined pulsar and continuum flux densities*   **b)** *The continuum flux densities*
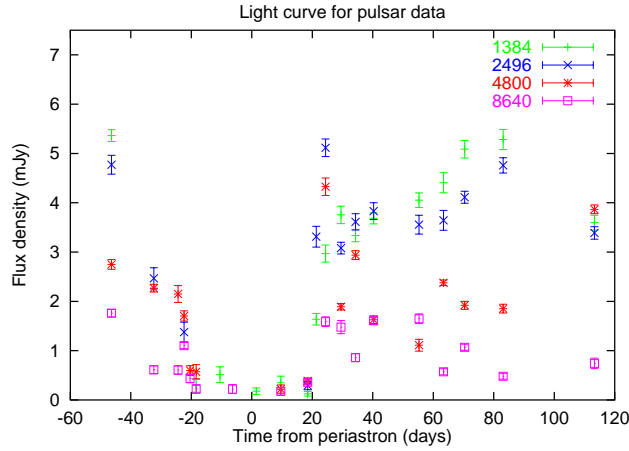
c) *The pulsar flux densities*

Figure 4.2: *Light curves from 2000 data*

4.1.2 Eclipse: frequency and time behaviour

When the scatter broadening is strong, flux from the unscattered on-pulse bins will spill over onto baseline bins, and we will not be able to see which bins are part of the baseline. The pulse profiles showed an exponential tail for the two components between $\mathcal{T} - 32$ and $\mathcal{T} + 19$, and in these situations, the baseline was chosen to only include the bins that had the least spill-over from the components. When the tail was not too long, we can still expect to be able to separate the pulsar flux from the continuum flux accurately, but once the tail increases too much, the pulsar flux will become underestimated, and the continuum flux overestimated (the errors involved are unquantifiable, so are not corrected for). Because of the very strong frequency dependence, a slight scattering at one frequency almost certainly means the components will not be detected in the lower frequencies.

Before periastron, the pulsar was detected at all frequencies at $\mathcal{T} - 46$, scattered at 2.5 GHz and not detected at 1.4 GHz at $\mathcal{T} - 32$, scattered at 4.8 GHz and not detected at 2.5 GHz at $\mathcal{T} - 24$, not detected at 1.4 GHz at $\mathcal{T} - 22$, not detected at 2.5 GHz at $\mathcal{T} - 20$ and $\mathcal{T} - 18$, and then not detected at any frequency until $\mathcal{T} + 10$. Additionally, the pulsar was observed once at the Parkes 64 m telescope at 1.4 GHz, and was detected at $\mathcal{T} - 29$.

After periastron, the pulsar was first detected at the ATCA, highly scattered, at 4.8 GHz at $\mathcal{T} + 10$, not detected at Parkes at $\mathcal{T} + 11$ or the ATCA at $\mathcal{T} + 13$. The pulsar was not detected at 2.5 GHz but detected at 4.8 GHz at $\mathcal{T} + 19$, however it was detected at Parkes at 1.3 GHz on the
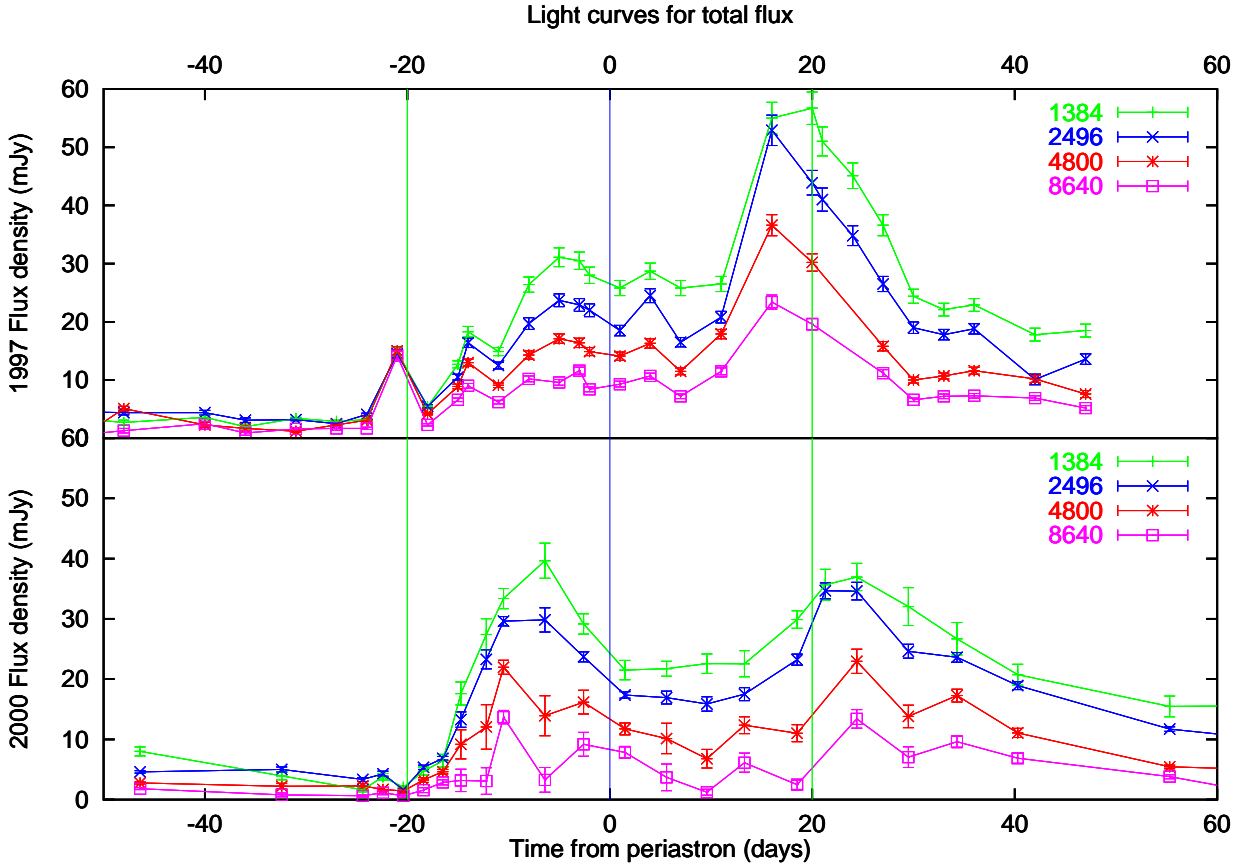
Figure 4.3: *Light curves from both 1997 and 2000 data on same scale. The vertical lines at $\mathcal{T} \pm 20$ are to enable easy comparison between the data, and are approximately when the pulsar becomes eclipsed in the 2000 data. The line at $\mathcal{T}$ is also to aid comparison. The combined flux density, rather than the continuum only, is plotted in the 2000 data, to ease comparison with the 1997 data.*

same day, and detectable at all frequencies from $\mathcal{T} + 21$ onwards. Therefore scattering was the main mechanism of eclipse until $\mathcal{T} - 16$, and then the large optical depth dominated until $\mathcal{T} + 6$, and then scattering again after this time.

The pulsar flux at 1.4 GHz rises slowly after coming out of eclipse (a similar effect is perhaps seen for 2.5 GHz) whereas the other frequencies rise immediately after first detection to their pre-periastron level and stay fairly constant. This implies the optical depth is still significant until 40 days after the eclipse has finished, and is enough to affect 1.4 GHz and 2.5 GHz, whereas the other frequencies suffer negligible effects, in accordance with equation 4.1. Some of the variability well away from the eclipse may be from long-term refractive scintillation (Johnston et al. 1996).

In 1997 the pulsar was detected with the ATCA until $\mathcal{T} - 21$ at all frequencies and at Parkes until $\mathcal{T} - 18$, then after periastron, detected from $\mathcal{T} + 16$ onwards. Before the periastron, the pulsar became scattered and then eclipsed earlier in 2000 than in 1997, and after periastron, emerged later than in 1997, suggesting the disk became either thicker or denser.

4.1.3 Continuum light curve

Description of light curve

In figure 4.2b, the continuum flux densities are shown. The continuum drops from being highly significant at $\mathcal{T} - 46$ (8 mJy at 1.4 GHz) to very low (2 mJy at 1.4 GHz) at $\mathcal{T} - 20$. The flux

24

density rapidly increases (to 40 mJy at 1.4 GHz) towards the first peak at $\sim \mathcal{T} - 6$. A decrease with a similar slope follows, between $\sim \mathcal{T} - 6$ and $\mathcal{T} + 2$. The flux density plateaus (at ~ 21 mJy at 1.4 GHz) at all frequencies between $\mathcal{T} + 1$ and $\mathcal{T} + 13$, and then rises again to a peak at $\sim \mathcal{T} + 22$. The rise to the second peak is slower than the first, and the subsequent fall is very slow (see table 4.2 for slopes). It takes approximately 40 days for the flux density at 1.4 GHz to significantly decrease, and it appears not to admit to a simple linear fit, needing instead perhaps 2 linear sections (table 4.2), or a decay of the form $a(t - t_0)^c$ (since synchrotron theory implies that the flux evolves as a power law with time). The flux seems to recover after falling steeply at $\mathcal{T} + 70$ at all frequencies. The continuum radiation clearly survives well after expected — the Ball et. al. (1999) model predicted no continuum emission at 1 GHz after $\sim \mathcal{T} + 65$. In future, the system will have to be studied well after $\mathcal{T} + 120$ to understand the late time behaviour, since the flux at the end of our observations is still well above pre-periastron levels.

| Frequency (MHz) | Linear fits (mJy/day) | | | | | $a(t - t_0)^c$ Fit for c |
| | First peak | | Second peak | | | Late time |
	Rise	Fall	Rise	Fall	Late time	
1384	3.6 ± 0.5	-2.2 ± 0.3	1.42 ± 0.04	-1.062 ± 0.009	-0.05 ± 0.04	-0.71 ± 0.12
2496	2.9 ± 0.6	-1.56 ± 0.02	1.5 ± 0.5	-0.79 ± 0.13	-0.06 ± 0.04	-1.4 ± 0.5

Table 4.2: *Fits to rise and fall of peaks in the continuum flux emission. See figure 4.4 for the fit for 2496 MHz.*
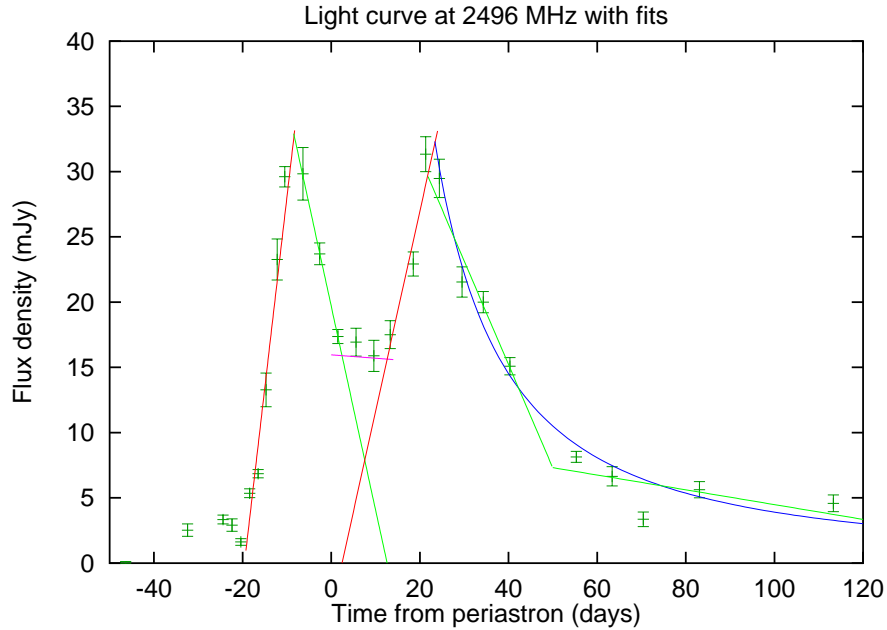

Figure 4.4: *Fits for the rise and fall times for 2496 MHz. The rise times are shown in red, and the linear fall times in green. The plateau resulting from the addition of the fall of the first peak and rise of the second is shown in purple. The "second peak fall" is the straight line between $\sim \mathcal{T} + 20$ and $\sim \mathcal{T} + 50$, and the "late-time fall" is the section from $\sim \mathcal{T} + 50$ onwards. Finally, the power law fit (excluding the attenuated flux at $\mathcal{T} + 70$) detailed in table 4.2 for late-time is shown in blue.*

Using the late-time fit for the intensity power law, we can get an average value of c from the two frequencies, and use appendix D.1 (specifically, equation D.6) to obtain a spectral index, and compare with the SI's in figure 4.5a. The average of c, taking into account the errors, is -0.75 ± 0.16, and implies $\alpha = -0.81$. This agrees very well with the continuum SI in the figure, and serves as a consistency check.

We fit the fall time of the first peak, and rise time of the second linearly, and add the slopes, and find the result is not inconsistent with the plateau between the peaks. Thus we can say the plateau is a result of just the flux from the two excited populations, without needing to find another physical process for acceleration or decay, and to fit another magnetic field.

Reconciliation with model

The pulsar first entered the disk at $\sim \mathcal{T} - 20$, where a combination of scattering and free-free absorption eclipsed the pulsar. Soon after, around $\mathcal{T} - 15$, non-relativistic electrons from the Be disk were accelerated in the newly created shock between the relativistic pulsar wind and the Be disk (see figure 2.2). The electrons were accelerated over a period of approximately 10 days. The synchrotron bubble was left behind as the pulsar moved behind the disk, and the bubble slowly evolved in the disk through synchrotron losses. The magnetic field at the first disk crossing site is expected to be lower than the second, because the pulsar is further from the Be star at this point, yet the short decay time indicates the electron population evolved quicker due to a higher magnetic field.

The light curve plateaus because the resultant flux is from addition of flux from both the first and second disk crossings (see figure 4.4 for an example), and the pulsar has already reentered the disk and causes another synchrotron bubble to form, before the first has completely decayed. The approximate equality of the fall and rise slopes of the first and second peaks respectively leads to the flatness of the plateau.

Once the excited electrons from the first disk crossing have completely decayed, the flux from the second peak continues to rise for another ~ 9 days until the peak at $\sim \mathcal{T} + 22$. The slow decay from the second peak indicates a low magnetic field, contrary to expectation, since the pulsar is closer to the Be star at this time.

The model makes a prediction that there is a sudden cutoff of the continuation of the first peak over ~ 10 days near $\sim \mathcal{T} + 55$ just after the end of the observations made in 1997. This cutoff was to show a frequency dependence. Even though the model can not be directly applied to this situation because the first peak died off quickly, in figure 4.2b, we can see all frequencies decrease sharply (from ~ 10 to ~ 5 mJy for 1384 MHz) at $\sim \mathcal{T} + 70$, but then recover. The data in this period is not sampled very well, so it is unclear as to what is happening, but we can see that at $\mathcal{T} + 113$ the continuum flux density at 1384 MHz is still $\sim 10\sigma$, and well above the level it was pre-periastron. Since this was the last observation made, it is unknown how long this excessive emission lasted for. However, the significant drop in flux at $\mathcal{T} + 70$ is possibly due to extra absorption at that time, rather than the predicted drop between $\sim \mathcal{T} + 50$ and $\mathcal{T} + 65$ followed by an unexplained recovery.

The expected cutoff length (the time between the start of decay of the second peak and the cutoff) as a function of frequency is given in appendix D.2 (specifically, equation D.10), which results in the 1.4 GHz cutoff length being ~ 2.5 times longer than at 8.6 GHz. Looking at the continuum light curve and data (figure 4.2b and table 4.1), we see the 8.6 GHz goes to zero within the error bars from $\sim \mathcal{T} + 63$ onwards, implying a possible cutoff at 1.4 GHz at $\sim \mathcal{T} + 128$. Before the cutoff time, the 1.4 GHz flux will be approximately constant (as evidenced by the late-time slopes in table 4.2), then within a period of ~ 10 days, the flux will drop to 0. Additionally, the cutoff length being 43 days at 8640 MHz implies an approximate magnetic field of ~ 1.8 G in the disk at the site of the bubble (the crossing time of $\sim \mathcal{T} + 20$ implies a distance of $\sim 50 R_c$ from the Be star), as long as the assumptions in appendix D.2 are valid. This is consistent with Ball et al. (1999), who claim the field strength is ~ 1 G in a more elaborate model.

Comparison with 1997

In figure 4.3, a comparison of the 1997 and 2000 data appear. It is apparent that the first peak is shifted earlier in time, and the second peak is later, similar to the behaviour of the pulsar during eclipse, as shown in section 4.1.2.

It was claimed in Ball et al. (1999), that the initial flat spectrum spike at $\mathcal{T} - 20$ in the 1997 data was a result of the pulsar splashing into the Be star disk. No such feature is apparent in the 2000 data, even though observations at this time were made every ~ 2 days explicitly to try to understand the spike. This suggests the spike was a transient event, rather than something associated with the general build-up of flux, as predicted in the model.

It was also claimed the first peak was smaller than the second, because the flux from the second peak was superimposed on the still-decaying first peak. The rise time of the two peaks (and fall time of the second peak) are almost equal in the 1997 data, and somewhat greater than the orbital crossing time (~ 3 days for $\sigma_d = 5°$), since the pulsar wind continues to interact with the Be disk either side of the encounter. The second peak decayed a lot faster than the first, because the magnetic field was higher at the interaction site, and so the synchrotron loss time was smaller.

With this periastron, the first peak has decayed completely before the second has reached its maximum, and so the fluxes are not superimposed on each other and hence the peaks are of similar height. The rise times and hence electron acceleration times of the two peaks are again ~ 10 days, although the rise time of the second peak is a little longer than the first implying the disk may be thicker at the site of the second crossing, but this is contrary to our view that the disk should be angled out with an opening angle of $\sim 5°$, and so the disk would be thicker further from the Be star. The extra thickness may be the result of clumpiness or a warpage in the disk. The first peak decays quicker than the second, also contrary to our expectations. According to the model, the decay time will always have a minimum length that is the same as its rise time, which appears to be the case for the first peak in the 2000 observations. The height of both peaks are of the order of the height of the first peak of the 1997 periastron, and the first peak has a similar rise time (although has a smoother rise). The flux in the second peak of both sets of data shows attenuation at 1.4 GHz relative to the 2.5 GHz data, possibly implying free-free absorption, and so the peak is ~ 1.5 times the measured flux density (assuming the other frequencies are not attenuated, and the flux follows the power law, equation 3.2) before absorption. This implies an optical depth of ~ 0.4 in the earlier parts of the second peak (at $\sim \mathcal{T} + 16$ in 1997, and $\sim \mathcal{T} + 22$ in 2000), and shows that the bubble has formed on the far side of the disk and the flux is being absorbed on its passage to Earth. The first peak in both sets of data is not attenuated at the lower frequencies by optical depth, as the synchrotron bubble forms on the side of the disk closer to Earth, and so does not have a high absorption.

The spreading of the light curve to earlier and later times for the first and second peaks respectively (along with the lengthening of the pulsar eclipse time), possibly implies the disk has become thicker since the system was observed 3 years ago, when the opening angle was $\sim 5°$, which is consistent with the expectation that Be stars have variable winds and accretion rates (Waters 1986).

4.1.4   Spectral indices

Ball et al. (1999) showed that the broad features of the spectral index of the 1997 data were in accord with their model. The spectral index of the continuum was predicted to be ~ -0.7 between $\mathcal{T} - 18$ and $\mathcal{T} + 20$, to steepen to ~ -1.1 during the second peak, and then to drop back to ~ -0.7 at $\mathcal{T} + 30$, thereafter continuing to smoothly decline.

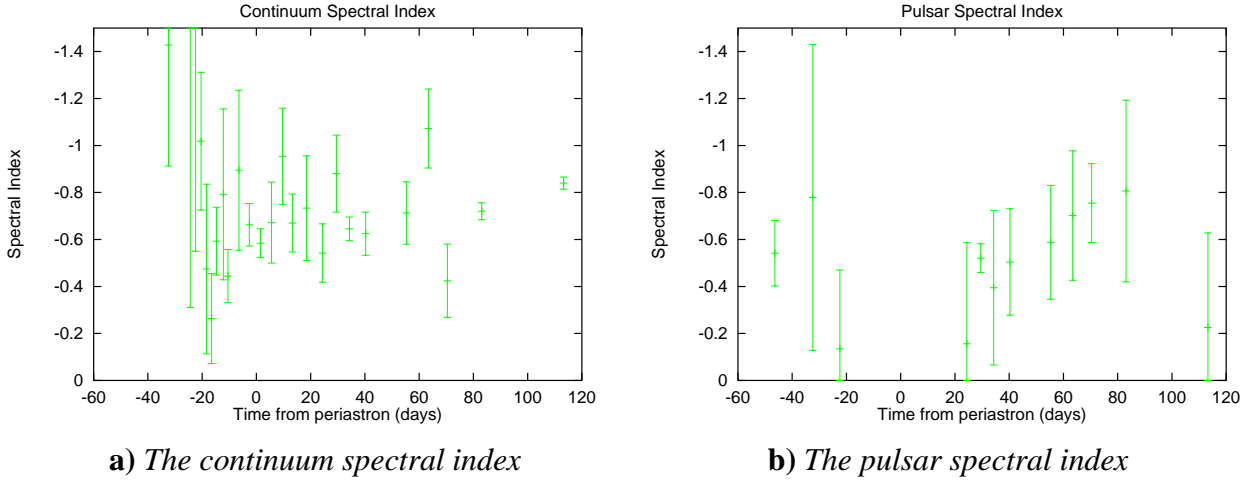**a)** *The continuum spectral index*   **b)** *The pulsar spectral index*

Figure 4.5: *Spectral indices from the 2000 data*

The spectral indices are shown in figure 4.5a for the continuum flux and figure 4.5b for the pulsar flux, for the 2000 periastron. The spectral index of the continuum is ~ -0.7 most of the time, and steepens to ~ -0.9 at $\sim \mathcal{T} + 30$, although this is not significant compared to the large error bars. There is perhaps a general trend to steepen from earlier times ($\mathcal{T} - 20$) to later times ($\mathcal{T} + 20$).

The error bars are larger than the data in 1997, and more realistic, because the fitting algorithm tries to take into account the errors associated with each flux (although only approximately, as discussed in section 3.3.5), rather than just relying on the fitting to obtain the error.

There was no prediction made for the pulsar spectral index, but it has a definite monotonically increasing trend at later times, due to the effect of the optical depth on the 1.4 GHz and 2.5 GHz data after eclipse.

Chapter 5

Results — Polarization

Polarization measurements enable us to obtain the rotation measure at various epochs around periastron, allowing us to determine the magnetic fields associated with the Be star. To understand the reliability of the linear polarization measurements, we need to first verify the circular polarization behaves as we expect it to, then we can determine whether the polarization calibration was correctly performed at the GPCAL stage.

We know from previous observations, as well as from the pulse profiles in figure 2.1, that the percentage circular polarization of the first pulse component is a lot less than the second. We also know that the fractional circular polarization is not affected by propagation as linear polarization is. We hence check that all observations have the same fractional circular polarization within the errors, for the first and second pulse components.

Additionally, since the linear polarization flux densities were obtained using the baseline subtracted data and UVFLUX, we can determine the reliability of all pulsar flux density measurements by verifying that the fractional circular polarization measurements are consistent, since all Stokes parameters are treated equally by the baseline subtraction process.

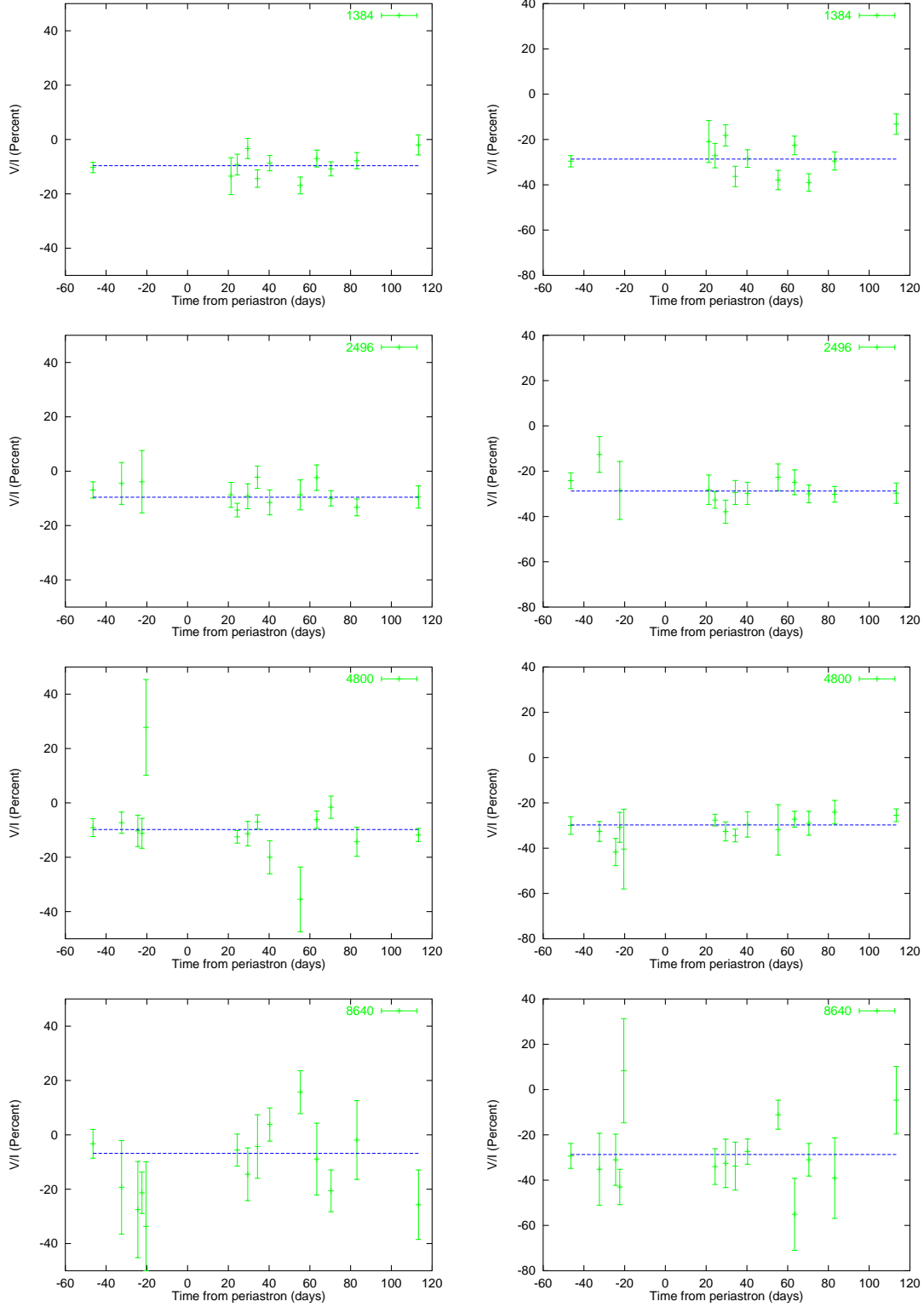## 5.1 Circular polarization

The fractional circularly polarized fluxes are presented in figures 5.1a and 5.1b, for the first and second components, respectively.

At the lower frequencies, the error bars are very small, of the order of $\sim 5\%$, and the errors in the higher frequencies are higher at $\sim 10\%$, since the flux density at 1.4 GHz is ~ 4 times the flux density at 8.6 GHz, assuming a spectral index of -0.8. All points are consistent with the mean, and the mean is in the range -6% to -10% for the first component at all frequencies, and between -28% and -30% for the second component at all frequencies, consistent with the values quoted in figure 2.1.

The agreement between the polarization obtained at Parkes (figure 2.1) and the entire set of observations here imply our UVFLUX measurements are reliable, giving us faith in our polarization calibration technique.

5.2 Rotation measure

The rotation measures were obtained for days when the pulsar flux was sufficiently strong (not eclipsed), and when the RM was not so high that the rotation angle across a small number of frequency channels (determined by the signal to noise ratio) was sufficient to depolarize the

a) *First pulse component.*

b) *Second pulse component. Note the different scale to the first component.*

Figure 5.1: *Percentage circular polarizations of pulsar for each frequency and time. Error bars are at the 1σ level, and the mean for each frequency and component is shown in blue.*

component. The rotation measure was obtained by combining as many channels as were necessary to obtain a sufficiently large S/N, and obtaining the polarization position angle for each of these channel groupings.

All rotation measures are presented in table 5.1, and rotation measure fits for various times

Date	(+$\mathcal{T}$)	Time (limits) (UT)	Rotation measures (rad m^{-2}) Frequency (GHz)				
			1.4	2.5	4.8	8.6	Average
Sep01	(-46.4)	00:30 – 01:30			-15900 ± 700	-13700 ± 2100	-15600 ± 700
		02:00 – 03:00			-12000 ± 900	-15800 ± 3200	-12400 ± 1000
		00:30 – 02:00			-16900 ± 3100	-15500 ± 900	-16600 ± 1700
		02:00 – 04:00			-12700 ± 500	-19600 ± 9700	-13700 ± 2500
		00:30 – 04:00			-14600 ± 1200	-15800 ± 2500	-14800 ± 900
Dec11	(55.3)	17:30 – 21:00	-107.6 ± 3.0	73 ± 16	470 ± 230		-105 ± 10
Dec19*	(63.4)	20:30 – 01:00			-6740 ± 660		-6740 ± 660
Dec26	(70.4)	19:00 – 23:50	-31.6 ± 3.2	32 ± 43	400 ± 280		-19 ± 18
Jan08	(83.1)	12:00 – 17:30	-47.9 ± 7.4	-3.8 ± 3.7	196 ± 170		-42.9 ± 7.7
Feb07	(113.3)	17:00 – 21:00	16 ± 19	-100 ± 16	-129 ± 15		12 ± 13

Table 5.1: *Rotation measure for various times and days (averaged over the two components, with each RM weighted as s^{-2}, where s is the error associated with the RM of that component). The RM obtained for each frequencies are first shown, then the averaged result (each frequency weighted in same way as above) is shown in the "Average" column. The entries with * next to them did not appear clean fits, despite the quoted errors, so ought to be discarded in further analysis.*

a) *4800 MHz, first time section*

b) *4800 MHz, third time section*

c) *8640 MHz, first time section*
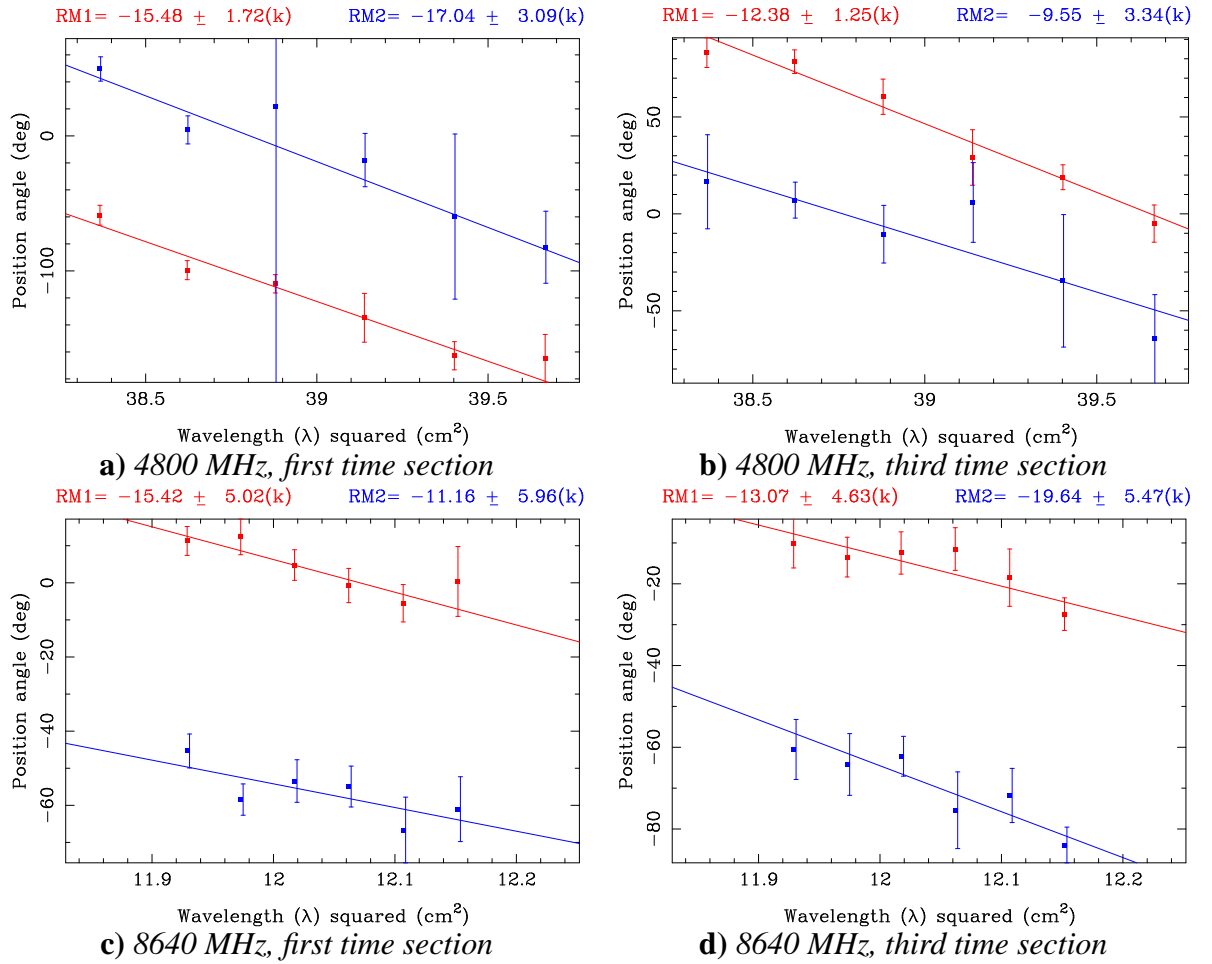
d) *8640 MHz, third time section*

Figure 5.2: RM's for different times and frequencies on September 1, when the polarization measurements were significant. The red and blue lines are for the first and second pulse component respectively. The values quoted are in k rad m^{-2}, and are directly imported into table 5.1. The larger the error for each individual point, the less weighting it gets in the fit. The position angle separation between the first and second components is near 90° in these fits, as expected.

during the September 1, 2000 observation ($\mathcal{T} - 46$) are presented in figure 5.2.

We use equation 3.1 to get the position angle of the linear polarization across the frequency bands, and then plot the position angle ϕ_λ against λ^2 and use equation 1.5 to obtain the RM,

but only for some of the observing bands. For high RM's, ϕ rotates too quickly, and the pulses appear depolarized within even just a single channel (width of 8 MHz at our observing resolution) allows, at the lower frequency bands (1384 and 2496 MHz). For small RM's, ϕ rotates too little for $\Delta\phi$ to be significant above the errors involved in measuring the linearly polarized flux densities, if too high a frequency is used (at 8640 MHz). Frequencies that depolarized the pulsar or gave an error in RM large compared to the actual RM calculated (because the frequency was too high for that RM) were not included in table 5.1 or the average.

The September 1 observation had particularly high S/N, and we expected the RM to be high and variable then, and so it was broken up into sections of about half an hour length each — the time observed at the 4.8 and 8.6 GHz receivers before switching to the next two. We measured the RM for each section that showed high enough S/N (the first and third sections), so the nature of the variability on time-scales of ~ 30 minutes could be obtained, and the results appear in entry one and two in the Sep01 block in table 5.1. We also use the other two sections to look at the behaviour over time-scales of ~ 2 hours (with the half hour gaps while the receiver was at the other frequencies), and the results appear in the third and forth entries in the table. The average RM from the entire observation is shown finally in the fifth entry, but if the RM is truly variable, this will not be physically meaningful. All other days have just the one time section, because the RM's showed less variability.

A further consistency check of both the polarization calibration and RM calculations can be made using the linear polarizations, by checking the change in position angle between the two components in the RM fits are $\sim 90°$ apart, since we know from previous data that the linear polarizations from the two components are orthogonal. Only data that had a constant separation of $\sim 90°$ between the two pulse components across the frequency band (such as those in figure 5.2) are included in table 5.1.

The extremely high RM of -16600 ± 1700 rad m^{-2} between 00:30 and 02:00 on September 1 is supported by the extensive error analysis and consistency checks, and represents the highest ever measured astrophysical RM.

5.3   Implications for B field

Using equation 1.4, we can estimate the mean magnetic field weighted as a function of density over the line of sight. Since the Be wind is the main contributer to the number density n, we can obtain a good estimate of the mean magnetic field just in this wind. At $\mathcal{T} - 46.4$, the pulsar was $87.5R_c$ from the Be star (where $1R_c$ is the stellar radius), and assuming a dispersion measure change (relative to the galactic value of 146.7 cm^{-3}pc) of ~ 0.2 cm^{-3}pc (we don't have a direct measurement of the DM for this time, and this is probably an upper limit) a magnetic field of 100 ± 10 mG is obtained for at least half an hour during the 4 hour observing period.

The high magnetic field resulting from the extreme RM, is possibly caused by a single clump of material contributing a highly organised magnetic field, rather than all of the wind in our line of sight to the pulsar contributing a semi-randomised magnetic field. The wind is fast flowing, so we expect random high density clumps that may lead to this situation. The clumpiness may also be the cause of the extra absorption of the continuum flux at $\sim \mathcal{T} + 70$.

Chapter 6

Conclusion

6.1   Light Curves and Model

Many observations of the 2000 periastron of the PSR B1259−63/SS2883 system were made at the ATCA, and the pulsar and continuum flux densities of the system were separated and analysed to give light curves for the pulsar and continuum emissions independently. The main features in the continuum light curve that differed from previous periastra were that the peak from the first disk-crossing decayed faster than the second, indicating a magnetic field anomalously higher in the first crossing, despite the pulsar being further from the Be star. The disk at the second crossing seems to be thicker than at the first crossing, because the rise time is longer, with the extra thickness possibly being the result of clumpiness or a warpage in the disk.

The pulsar eclipse started earlier, and finished later in 2000 than in 1997, and the continuum emission was similarly spread out, so we expect the disk opening angle had increased from its former value of $\sim 5°$.

Optical depth was an important feature not only for the pulsar emission during deep eclipse, but for the continuum emission after the pulsar started emerging from the disk, indicating the synchrotron bubble formed on the far side of the disk, and was "peeking through". Scattering broadened the pulses near the edges of eclipse, and the highly variable pulsar flux at other times (in the higher frequencies) was caused by long term refractive scintillation.

Additionally, analysis of the synchrotron cutoff length at 8.6 GHz reveal the magnetic field in the disk at $\sim 50 R_c$ from the Be star, as being approximately 1.8 G.

6.2   Rotation Measures and Magnetic Field

Far from the Be star (after $\mathcal{T} + 55$, when the pulsar was $> 100 R_c$ from the Be star), the RM was low — of the order of -100 rad m^{-2}. Closer to the Be star (time $\mathcal{T} - 46.4$, distance $87.5 R_c$), the pulsar attained the highest measured astrophysical RM of -16600 ± 1700 rad m^{-2} during part of the September 1 observation, implying a magnetic field of at least 100 ± 10 mG at this distance, in the Be wind. The high average magnetic field could be the result of clumping in the high velocity wind, reducing the washout of the magnetic field over the line of sight.

6.3   Future Prospects

There are many things that could follow on from this project. The 1997 data, while using the older correlator, still was observed in a pulsar binning mode, with 8 time bins (4 on, 4 off-pulse). An attempt could be made to separate the pulsar from the continuum emission, using

the programs developed here. This could be harder, and would result in an overestimation of the continuum emission and underestimation of the pulsar flux (Johnston et al. 1999), although for different reasons than that quoted in section 4.1.2 for our analysis. We could then produce light curves for the pulsar and continuum emission separately, but more importantly, obtain RM's for various times during the 1997 periastron.

The distance of ~ 1.5 kpc implies an angular diameter of the orbit ~ 4 mas (Johnston et al. 1999). Observing the system using Very Long Baseline Interferometry (VLBI), we could obtain the size of, and hence an accurate distance measurement to the system. Preliminary observations are already underway. We could also obtain proper motions of the system, and verify that the system is relatively slowly moving. Although we expect the system got a large momentum kick at the supernova stage, the Be star is very heavy, so would slow the system down to only ~ 100 km s^{-1}.

The next periastron is in April 2004. It seems we may have to observe until at least $\mathcal{T} + 140$ to see the cutoff at 1.4 GHz. The upgrade of the ATCA to 12 and 24 GHz also provides us with an opportunity to monitor the eclipse at these higher frequencies. Although the flux density is likely to be low, these observations may be able to constrain the synchrotron spectrum by showing evidence for the high frequency cut-off not present in the current data. Observations of the pulsar at 12 GHz where optical depth and scattering are much reduced may enable us to track it deeper into the eclipse.

Finally, we have been able to fit the rate of acceleration and decay to the peaks in the continuum light curve, but more modelling of this system remains to be done. We have only done a small amount of the analysis necessary to obtain magnetic fields in the disk, which is of a different form to the magnetic field in the Be wind, and our cutoff times are only approximate.

REFERENCES

Atoyan A. M., 1999, AA, 346, L49

Baade W., Zwicky F., 1934a, Proc. Nat. Acad. Sci., 20, 254

Baade W., Zwicky F., 1934b, Phys. Rev. , 45, 138

Ball L. T., Melatos A., Johnston S., Skjaeraasen O., 1999, ApJ, 514, L39

Bhattacharya D., van den Heuvel E. P. J., 1991, Phys. Rep. , 203, 1

Buil C., 2000, The Be stars Corner. `<url:http://www.astrosurf.com/buil/us/bestar.htm>`

Clingempeel R. K., 2001. *Stellar classifications*, `<url:http://business.fortunecity.com/rowling/167/SuperNovae/Classifications.%html>`

Cominsky L., Roberts M., Johnston S., 1994, ApJ, 427, 978

Cordes J. M., Weisberg J. M., Boriakoff V., 1985, ApJ, 288, 221

de Loore C., de Greve J. P., Vanbeveren D., 1978, AA, 67, 373

Gold T., 1968, Nat, 218, 731

Gold T., 1969, Nat, 221, 25

Harrison E. R., Tademaru E., 1975, ApJ, 201, 447

Hewish A., Bell S. J., Pilkington J. D. H., Scott P. F., Collins R. A., 1968, Nat, 217, 709

Hirayama M., Nagase F., Tavani M., Kaspi V. M., Kawia N., Arons J., 1996, Proc. Astr. Soc. Jap., 48, 833

Johnston S., 1995, Curr. Sci., 69, 521

Johnston S., Lyne A. G., Manchester R. N., Kniffen D. A., D'Amico N., Lim J., Ashworth M., 1992, MNRAS, 255, 401

Johnston S., Manchester R. N., Lyne A. G., Nicastro L., Spyromilio J., 1994, MNRAS, 268, 430

Johnston S., Manchester R. N., Lyne A. G., D'Amico N., Bailes M., Gaensler B. M., Nicastro L., 1996, MNRAS, 279, 1026

Johnston S., Manchester R. N., McConnell D., Campbell-Wilson D., 1999, MNRAS, 302, 277

Johnston S., Wex N., Nicastro L., Manchester R. N., Lyne A. G., 2001, MNRAS, In Press

Kaspi V. M., Johnston S., Bell J. F., Manchester R. N., Bailes M., Bessell M., Lyne A. G., D'Amico N., 1994, ApJ, 423, L43

Kaspi V. M., Tavani M., Nagase F., Hirayama M., Hoshino M., Aoki T., Kawai N., Arons J., 1995, ApJ, 453, 424

Kaspi V. M., Tauris T., Manchester R. N., 1996, ApJ, 459, 717

Kennel C. F., Coroniti F. V., 1984, ApJ, 283, 694

Lewin W. H. G., van den Heuvel E. P. J., eds, 1983, Accretion–driven stellar X-ray Sources. Cambridge University Press, Cambridge

Lyne A. G., Smith F. G., 1968, Nat, 218, 124

Lyne A. G., Ritchings R. T., Smith F. G., 1975, MNRAS, 171, 579

Manchester R. N., Johnston S., 1995, ApJ, 441, L65

Manchester R. N., 2001, Pasa, 18, 1

McClusky G. E., Kondo Y., 1971, Astrophys. Space. Sci., 10, 464

Melatos A., Johnston S., Melrose D. B., 1995, MNRAS, 275, 381

Melrose D. B., Ball L. T., 1996, in *Plasma & Astrophysics*, Lecture notes

Melrose D. B., McPhedran R. C., 1991, Electromagnetic processes in dispersive media. Cambridge University Press, Cambridge

Melrose D. B., 1996, in Johnston S., Walker M. A., Bailes M., eds, Pulsars: Problems and Progress, IAU Colloquium 160. Astronomical Society of the Pacific, San Francisco, p. 139

Oppenheimer J. R., Volkoff G., 1939, Phys. Rev. , 55, 374

Pacini F., 1968, Nat, 219, 145

Reifenstein E. C. I., Brundage W. D., Staelin D. H., 1969, Phys. Rev. Lett., 22, 311

Sault R. J., Killeen N. E. B., 1998, The Miriad User's Guide. Australia Telescope National Facility, Sydney, `<url:http://www.atnf.csiro.au/computing/software/miriad/>`

Smith F. G., 1977, Pulsars. Cambridge University Press

Staelin D. H., Reifenstein III E. C., 1968, Sci, 162, 1481

Tauris T. M., Bailes M., 1996, AA, 315

Tavani M., Arons J., 1997, ApJ, 477, 439

Tavani M., Arons J., Kaspi V. M., 1994, ApJ, 433, L37

Taylor J. H., Fowler L. A., McCulloch P. M., 1979, Nat, 277, 437

Turlo Z., Forkert T., Sieber W., Wilson W., 1985, AA, 142, 181

Underhill A., Doazan V., 1982, B Stars With and Without Emission Lines. NASA SP-456, Washington

van den Heuvel E. P. J., de Loore C., 1973, AA, 25, 387

van Kerkwijk M. H., 1993, PhD thesis, University of Amsterdam

Waters L. B. F. M., 1986, AA, 162, 121

Waters L. B. F. M., Coté J., Lamers H. J. G. L. M., 1987, AA, 185, 206

Wex N., Johnston S., Manchester R. N., Lyne A. G., Stappers B. W., Bailes M., 1998, MNRAS, 298, 997

Young M. D., Manchester R. N., Johnston S., 1999, Nat, 400, 848

Appendix A

Data analysis Tasks

Command	Arguments/Example	Description/Notes

DO_LOAD[1]	*fmt:* `<day> <input-files ....>`
	
	`do_load sep01`
	`/cdrom/DATA/2000-09-01_*.C326`
		Loads all the files provided on the command line, naming them according to the "day" provided. This provides a consistent naming scheme that should give unique file names for each observing session. The flags provided to MIRIAD's ATLOD are correct as of the time of publication, and take into account a bug that was discovered in the correlator setup around the observing time.

DO_CAL[2]	*fmt:* `<day> <reference-antenna>` `do_cal sep01 3`	This tries to automatically flag everything above 6σ, but quite often, all the data for a baseline was very noisy, and so manual flagging (using MIRIAD's TVFLAG or BLFLAG) and rerunning this script was necessary. After flagging, it recalculates the calibration tables for secondary calibrator and source.
DO_FIX[3]	*fmt:* `<day> <DM>` `do_fix sep01 146.7`	Removes the effect of dispersion across the receiver frequency band. Provide the DM either by guessing and then subsequently improving the values, or making use of an observation at another telescope that can determine the DM.

---

[1]Does not delete the output files before creating them. Delete them before rerunning.

[2]Properly deletes the calibration tables first, then flags and recalibrates.

[3]Checks dependencies, and if files need updating, updates them, otherwise leaves them. Relies on file timestamps (hence, make sure system time is correct).

[4]Automatically run as part of the GENERATEFLUXERRTABLE.PL, GENERATECIRCERRTABLE.PL or GENERATERMTABLE.PL scripts as appropriate.

[5]Needs to know the offset of the pulsar from the pointing centre, by providing an "offsets.txt" file (section B.2)

[6]This program does some lengthy calculations, so caches the result in a file in the "cached" directory underneath the current directory, and reuses it if the source file hasn't changed for next time. It makes sure no script gets confused by giving the script a different arguments from the last time it was run (such as which channels were selected), by storing that information in the cached file name. It may also store a lot of postscript files used in fitting in the "ps" directory.

[7]The arguments in square brackets are optional. Any optional argument before an optional argument you want to supply also has to be supplied.

Command	Arguments/Example	Description/Notes
DO_PSRBL[3,4]	*fmt:* `do_psrbl`	Subtracts the average of the baseline bins provided in the binsl.txt file (see section B.1), to separate continuum from pulsed flux.
DO_AVER[3,4]	*fmt:* <day> `do_aver sep01`	Averages the pulsar bin data bins together. The use of this significantly speeds up any processes that don't need the bin data later on. It does the averaging for both the baseline subtracted data (in which case the average becomes the pulsar flux), or the combined data.
DO_IMAGE[3,4,5]	*fmt:* <day> <all | psr | allimg> `do_image sep01 allimg`	Images the given file or files, making appropriate decisions about cell size etc, for the PSR B1259−63 source. Images the full flux when "all" selected, pulsar flux when "psr" selected, and both when "allimg" selected.
DO_IMFIT[3,4,5]	*fmt:* <day> <all | psr | allimg> `do_imfit sep01 allimg`	Fits the flux of a point source, looking at only the pulsar or full flux. Fits the full flux when "all" selected, pulsar flux when "psr" selected, and both when "allimg" selected.
DO_UVFLUX[3,4,5,6,7]	*fmt:* <day> [<format>] [<time>] [<channels>] [<freq>] `do_uvflux sep01`	Fits a point source in the UV data, looking at only the pulsar or full flux. If the argument "format" is supplied, then if it is "2" then the fit is done for both Stokes V and I, otherwise it just fits I. If the "time" argument is given and is "hh1:mm1,hh2:mm2", then the fit is done for times hh1:mm1 to hh2:mm2 UT. If the "channel" argument is given and is "a,b", the fit is done for just the channels a to $a+b-1$. If the argument "freq" is given, the fit is just done for the single frequency given.

DO_UVFLUXRM[3,4,5,6,7]	*fmt:* <day> [<time>] [<channels>] [<bins>] [<freq>]
	
	`do_uvfluxrm sep01 12:00,13:00 11,2`
	`16,16,1,2 1384`
		Fits a point source in the UV data, looking at only the pulsar linearly polarized fluxes (U and Q) in a limited range of channels, pulsar bins, time and frequencies. If the "time" argument is given and is "hh1:mm1,hh2:mm2", then the fit is done for times hh1:mm1 to hh2:mm2 UT. If the "channel" argument is given and is "a,b", the fit is done for just the channels a to $a + b - 1$. If the argument "freq" is given, the fit is just done for the single frequency given. And if the "bin" argument is given and is "$a_1,b_1,[a_2,b_2]...$", then the bins are selected in pairs a_1 to b_1, a_2 to b_2 etc.

DO_UVFLUXINDIVPULSE[3,4,5,6,7]	*fmt:* <day> [<format> [<pulse>]] `do_uvfluxindivpulse sep01 2 1`	Fits a point source in the UV data, looking at only the pulsar I and V fluxes. If the "format" argument is given and is "2", then the fit is done for both I and V, otherwise it is just done for I. If the "pulse" argument is given, then we only fit for that pulse number, using the binsl.txt file (see section B.1), otherwise we fit for the whole pulse profile.

Command	Arguments/Example	Description/Notes
GENERATEFLUXERRTABLE.PL	*fmt:* `generatefluxerrtable.pl`	Run from the root directory, and gives a table of all of the fluxes in the directories below of the form yyyy-mm-dd that have a binsl.txt file present, signifying that the data in that directory has been reduced. This also generates the cont+psrfluxes?.txt, contfluxes?.txt and psrfluxes?.txt files, which are used in the generation of the light curve plots.
GENERATECIRCTABLE.PL	*fmt:* `generatecirctable.pl`	Run from the root directory, and gives a table of all of the fractional circularly polarized fluxes for the pulsar, for the whole profile, the first component, and the second component. Goes through the directories below of the form yyyy-mm-dd that have a binsl.txt file present, signifying that the data in that directory has been reduced. This also generates the psr-Vfluxes?.?.txt files, which are used in the generation of the fractional circularly polarized plots.
GATHERRMS.PL	*fmt:* `-d <date> [-noprogrun 1] [-fq <listfreqs:1..n> -t <timelist> -b1 <bins,component1-f1,f2,...,fn> -b2 <bins,component2-f1,f2,...,fn>] [-divs <divs1...divns>]` `gatherrms.pl -d sep01 -b1 12,12 6,6 -b2 1,1 11,11 -fq 4800 8640 -t 00:30,01:30 02:00,03:00 00:30,02:00 02:00,04:00 00:30,04:00 -divs 6`	Goes through each frequency provided, and gets the RM from both pulse components. For each frequency within the time division, the RM's are averaged, once the user is asked whether they want to include the current fit (may not want to if it looks hopeless). The program stores a history file (rmhistory.txt), so that old parameters are easily restored, and outputs a LATEX file and postscript images so that the fits can be viewed and saved. It also outputs the fits to "rmfit.dat" for later use. You can have an excludeplotrm.txt file to easily exclude bad plots every time the program is run. The format is given in section B.3. Turn the -noprogrun switch on, if you don't want to generate the fits and plots — you just want to regenerate the LATEX file.

Command	Arguments/Example	Description/Notes
CALCSI.PL	*fmt:* `<all|cont|psr>` `calcsi.pl psr`	Plots and then fits the spectral indices for the combined flux, continuum or pulsar, for all days individually, making use of the CALCSI.GNUPLOT script in GNUPLOT to do the fitting, using the GNUPLOT "fit" routine to fit a straight line in log-log space.
GNUPLOT *SIS.GNUPLOT	*fmt:* `<cont+psrsis.gnuplot| contsis.gnuplot| psrsis.gnuplot>` `gnuplot scripts/cont+psrsis.gnuplot`	Plots the spectral indices for all days, for either the combined flux, the continuum, or just the pulsar. Makes use of the output of the CALCSI.PL scripts.
GNUPLOT CIRC?.GNUPLOT	*fmt:* `<circ0.gnuplot| circ1.gnuplot| circ2.gnuplot>` `gnuplot scripts/circ2.gnuplot`	Plots the fractional circular polarisation of the pulsar flux. If using circ0.gnuplot, the whole pulse profile is used, else the first and second pulse components are used for circ1.gnuplot and circ2.gnuplot respectively.
GNUPLOT LIGHTCURVES*.GNUPLOT	*fmt:* `<lightcurvescont+psr.gnuplot| lightcurvescont.gnuplot| lightcurvespsr.gnuplot>` `gnuplot scripts/lightcurvescont+psr.gnuplot`	Plots the light curve for all days, for the pulsar, continuum or combined fluxes.

Table A.1: *Table of scripts produced to analyse data for 2000 periastron. These are run in order, interspersed with manual tasks that need to be performed using* MIRIAD *tasks. Some of these programs use files that are documented in appendix B.*

Appendix B

Input file formats

B.1 BINSL.TXT format

The format of the binsl.txt file follows along with an example:

#Comments begin with hash	
obs date (yyyy-mm-dd)	2000-09-01
array name	6A
# User error is redundant now, but must still	
# be included (just set to 0)	
freq1: usererror	1384: 0
freq2: usererror	2496: 0
freq3: usererror	4800: 0
freq4: usererror	8640: 0
# If the pulsar is clearly visible, we want to	
# include it in the output tables and lightcurve,	
# so set 1. Else set 0. If set to zero,	
# following paramaters are ignored. Hence just	
# set the baseline to "0,0", and the pulses to	
# "0,0 - 0,0"	
freq1 psr visible?	1
freq2 psr visible?	1
freq3 psr visible?	1
freq4 psr visible?	1
freq1 baselines	2,3,9,12
freq2 baselines	1,1,7,8,14,15
freq3 baselines	4,8,14,16
freq4 baselines	1,3,7,10,14,16
# onpulse bins (for circ polarization only.	
# RM calculations are done by entering	
# into script manually).	
freq1 first pulse on bins – second pulse on bins	13,16,1,1 - 4,8
freq2 first pulse on bins – second pulse on bins	2,6 - 9,12
freq3 first pulse on bins – second pulse on bins	11,13 - 1,3
freq4 first pulse on bins – second pulse on bins	4,6 - 11,13

B.2   OFFSETS.TXT format

The offsets.txt file just contains the position offset of the pulsar relative to the observing centre. Most of the time, the file will not be necessary (it will be set to a default of "0.0,-30.0" if not present, but if it is present, and contains a line such as "0.0,-60.0", then this will define the new position of the pulsar, relative to the observing centre, in arcsec, and with the same sign convention as used by MIRIAD tasks such as INVERT.

B.3   EXCLUDEPLOTRM.TXT format

If you know that a certain combination of frequencies, pulse number, number of channel divisions and time gives a useless fit of the RM, you can exclude it every time you use the GATHERRMS.PL script, by including a file with the name of "excludeplotrm.txt" with lines of the format:

   <freq> <number channel divisions> <1st bin selection> <2nd bin selection> <time>

An example below:

4800 6 12,12 1,1 00:30,01:30
4800 6 12,12 1,1 02:30,03:30

Appendix C

Polarization angle error: Bias calculation

The quantity in the denominator of equation 3.4 involves two squared quantities with associated errors. The quantities hence can never be less than 0, and so the expectation values of the denominator is not 0 when Q and U are both 0 in reality. So we subtract the expectation value of $\sqrt{(Q + \Delta Q)^2 + (U + \Delta U)^2}\big|_{\substack{Q=0 \\ U=0}}$ from the denominator to get a better approximation for the error in ϕ when the polarized fluxes involved are low.

The expectation value of $(\Delta Q)^2$, assuming Gaussian errors in Q is:

$$
\begin{aligned}
\langle (\Delta Q)^2 \rangle &= \frac{\displaystyle\int_0^\infty (\Delta Q)^2 e^{-\left(\frac{\Delta Q}{\Delta Q_{\mathrm{uvflux}}}\right)^4} \mathrm{d}(\Delta Q)}{\displaystyle\int_0^\infty e^{-\left(\frac{\Delta Q}{\Delta Q_{\mathrm{uvflux}}}\right)^4} \mathrm{d}(\Delta Q)} \\
&= (\Delta Q_{\mathrm{uvflux}})^2 \frac{\Gamma(3/4)}{4\Gamma(5/4)} \\
&\approx 0.338 (\Delta Q_{\mathrm{uvflux}})^2
\end{aligned}
\tag{C.1}
$$

where $\Delta Q_{\mathrm{uvflux}}$ is the error calculated from UVFLUX. Combined with an identical calculation for $(\Delta U)^2$, the expectation value of $\sqrt{(Q + \Delta Q)^2 + (U + \Delta U)^2}\big|_{\substack{Q=0 \\ U=0}}$ is $\sqrt{2 \times 0.338 \Delta_{\mathrm{uvflux}}^2} = 0.822\Delta_{\mathrm{uvflux}}$, assuming equal errors of Q and U in UVFLUX. We subtract this value from the denominator in equation 3.4 to give

$$
\Delta \phi = \left| \frac{0.5\Delta}{L - 0.822\Delta} \right|
\tag{C.2}
$$

Appendix D

Synchrotron Bubble Evolution

D.1 Source intensity as a function of frequency and time

The synchrotron bubble model has a source expanding isotropically. In this case, the energy of the particles are $\epsilon \propto L^{-1}$ where L is the scale length of the source. If the source expands at a constant speed, then $\epsilon = \epsilon_0(t_0/t)$, where the energy is ϵ_0 at time t_0. If there is not a continuing supply of radiating electrons, the total number of electrons remain constant, and the evolution of the number density at a given energy and time is (Melrose & Ball 1996):

$$N(\epsilon, t) = K(t)\epsilon^{-a} = K_0 \left(\frac{t}{t_0}\right)^{-(a+2)} \epsilon^{-a} \tag{D.1}$$

We can substitute this form of $K(t)$ into

$$\langle I(\nu) \rangle = A(a) L K (mc^2)^{1-a} \frac{\epsilon^2 \nu_B}{4\pi\epsilon_0 c} \left(\frac{2\nu}{3\nu_B}\right)^{-(a-1)/2} \tag{D.2}$$

where ν_B is the cyclotron frequency, and is given by:

$$\nu_B = \Omega_e/2\pi = 2.8 \times 10^6 \left(\frac{B}{1\text{G}}\right) \text{Hz} \tag{D.3}$$

and $A(a)$ is a dependent only on a, and for a spectral index α (where α is defined oppositely to equation 3.2) of 1.5, $A(a) = 0.073$, and $\nu_B \propto B \propto L^{-2} \propto t^{-2}$. Ignoring all constants, we get, from equation D.2:

$$\langle I(\nu) \rangle \propto \nu^{-(a-1)/2} t^{-2(a+1)} \tag{D.4}$$

We can approximate the a in the electron energy spectrum power law $N(\epsilon) = K\epsilon^{-a}$ by the spectral index α in the observed spectral power law by

$$a = 2\alpha + 1 \tag{D.5}$$

This finally gives us the evolution of the synchrotron bubble before cutoff:

$$I(\nu) \propto \nu^{-\alpha} t^{-4(\alpha+1)} \tag{D.6}$$

where t is really the difference in time between the time of acceleration t_{accel} and the current time t. i.e. $t \to (t - t_{\text{accel}})$.

44

D.2 Synchrotron cutoff times

There is a break in the synchrotron emission spectrum, and at lower energies than the break, $N(\epsilon, t) \propto \epsilon^{-a}$, and above the cutoff, $N(\epsilon, t) \propto \epsilon^{-(a+1)}$.

Now, the electron half lifetime is given by (Melrose & Ball 1996):

$$t_{1/2} = \frac{1}{b\epsilon} = 5 \times 10^8 \frac{1}{\sin^2 \alpha} \left(\frac{B}{1\mathrm{G}}\right)^{-2} \left(\frac{\epsilon}{mc^2}\right)^{-1} \quad \text{seconds} \tag{D.7}$$

where α is the half angle of the cone of emission. We can not know α, so we approximate $\sin^2 \alpha$ by its expectation value 2/3. The energy at which the spectral break occurs is when the half lifetime is equal to the time elapsed. After this time, the emission at the relevant frequency will drop to zero very quickly — and so we call this the cutoff time.

We approximate the energy of the particles ϵ by:

$$\epsilon \approx mc^2 \left(\frac{2\pi m \nu}{0.47 eB \sin\theta}\right)^{1/2} \tag{D.8}$$

where θ is the angle to the observer, and now we approximate $\sin\theta = 1$ to get a calculation hopefully correct to an order of magnitude — the important feature being the $\sqrt{\nu}$ dependency.

Hence, we can finally say

$$t_{\mathrm{lifetime}} \approx 5 \times 10^8 \times 3/2 \times B^{-2} \times \left(\frac{0.47 \times 1.6 \times 10^{-19}}{2\pi \times 9.11 \times 10^{-31}} \frac{B/10^4}{\nu}\right)^{1/2} \quad \text{seconds} \tag{D.9}$$

where the magnetic field B is in Gauss. i.e,

$$t_{\mathrm{cutoff}} - t_{\mathrm{accel}} \approx \frac{315}{\sqrt{B^3 \nu}} \quad \text{days} \tag{D.10}$$

where B is in Gauss, and ν is in GHz.